https://doi.org/10.5194/egusphere-2026-479
Preprint. Discussion started: 29 January 2026

Opposing entrainment effects of cloud droplet sedimentation during the pre-breakup stage of the stratocumulus to cumulus transition

Moritz Schnelke[1], Maike Ahlgrimm[2, 3], and Anna Possner[1]

[1]Institute for Atmospheric and Environmental Sciences, Goethe University Frankfurt, Frankfurt am Main, Germany
[2]Deutscher Wetterdienst, Offenbach am Main, Germany
[3]Hans-Ertel-Zentrum für Wetterforschung, Offenbach am Main, Germany

Correspondence: Moritz Schnelke (schnelke@iau.uni-frankfurt.de)

Abstract. Cloud droplet sedimentation is known to influence the evolution of the stratocumulus-topped boundary layer by reducing entrainment. Although this mechanism is well studied regarding the early evolution of stratocumuli, its sustained effects over longer timescales remain largely unexplored. Here, we use large-eddy simulations to investigate how sedimentation influences stratocumulus development in the context of the stratocumulus to cumulus transition. We conduct $48\,\mathrm{h}$ long simulations of 10 transects in the Northeast Pacific, covering the full deepening stage before cloud breakup. All sedimentation cases show the previously reported initial reduction in entrainment, whereas the later stages reveal different effects depending on the cloud's liquid water path (LWP). While the more frequent precipitating, high-LWP (LWP $> 50\,\mathrm{g\,m^{-2}}$) cases continue to exhibit weaker entrainment, the non-precipitating, low-LWP (LWP $\leq 50\,\mathrm{g\,m^{-2}}$) cases reverse the initial effect and show stronger entrainment. In those radiatively unsaturated low-LWP clouds, the increase in LWP due to the initial entrainment reduction initiates a feedback chain that amplifies LWP, longwave cooling, and turbulent circulations in the boundary layer, ultimately leading to increased entrainment. Initial studies showed that droplet sedimentation reduces entrainment in short ($\leq 6\,\mathrm{h}$) simulations of low-LWP clouds, which has been extrapolated in the literature to all stratocumuli on much longer timescales. Our results suggest that this extrapolation is indeed correct in common high-LWP clouds, although it had previously been inferred from the rare low-LWP regime, where the opposite is found. Meanwhile, we find that cloud breakup remains largely unaffected across the transition.

1 Introduction

Stratocumulus clouds are an important contributor to Earth's cooling, as they reflect a high amount of incoming shortwave radiation and have only little effect on outgoing longwave radiation (Wood, 2012). The marine type occurs frequently over the midlatitude oceans as well as the eastern basins of subtropical oceans (Klein and Hartmann, 1993; Wood, 2012). Subtropical stratocumulus clouds often organise in vast semi-permanent decks near the coasts, which gradually break up as they are advected over warmer waters in the direction of the free ocean (Klein and Hartmann, 1993; Sandu et al., 2010). This phenomenon is known as the stratocumulus to cumulus transition (SCT). The SCT has been studied extensively in the past decades using observations (e.g. Zhou et al., 2015; Eastman and Wood, 2016; Wood et al., 2018; Bretherton et al., 2019; Mohrmann et al., 2019; Sarkar et al., 2019; Christensen et al., 2020) as well as numerical simulations (e.g. Krueger et al., 1995; Bretherton and

https://doi.org/10.5194/egusphere-2026-479
Preprint. Discussion started: 29 January 2026

Wyant, 1997; Wyant et al., 1997; Sandu et al., 2010; Sandu and Stevens, 2011; De Roode et al., 2016; Yamaguchi et al., 2017; Blossey et al., 2021; Erfani et al., 2022). The main dynamical driver is the rising sea surface temperature (SST) that promotes decoupling of the stratocumulus deck from the surface. Cumulus clouds start to form in a mixed layer below cloud base and subsequently penetrate into the above-lying deck. Increased entrainment together with overshooting cumuli eventually leads to the dissipation of the stratocumulus deck and its replacement by shallow cumuli (Bretherton and Wyant, 1997; Wyant et al., 1997).

While this dynamical mechanism is widely accepted, it has been shown in recent years that the SCT is also influenced by microphysically induced processes like precipitation. Numerical studies utilising LES are largely in agreement that precipitation can have an accelerating impact on the SCT (Sandu and Stevens, 2011; Yamaguchi et al., 2017; Blossey et al., 2021; Erfani et al., 2022). In Yamaguchi et al. (2017), the authors even found a precipitation-driven transition through drizzle formation in the sub-cloud layer cumuli, that cleanses the stratocumuli from aerosols in a positive feedback loop. In contrast, most observational studies remain inconclusive about the effect of precipitation due to the challenge of disentangling individual mechanisms (Zhou et al., 2015; Eastman and Wood, 2016; Mohrmann et al., 2019; Sarkar et al., 2019).

One mechanism impacting two key drivers of the SCT, precipitation and cloud-top entrainment (hereafter entrainment), is cloud droplet sedimentation. This process has been neglected until Ackerman et al. (2004) reported on the reduction of the entrainment velocity in stratocumulus clouds in large-eddy simulations (LES), when including droplet sedimentation. This was confirmed and further quantified by Bretherton et al. (2007); Wyant et al. (2007); Ackerman et al. (2009); Hill et al. (2009). The main reason is that the removal of cloud droplets from the entrainment zone reduces the evaporation rate, which in turn slows down the entrainment rate. More recently, the analysis was extended using direct numerical simulations (DNS) by de Lozar and Mellado (2017); Schulz and Mellado (2019); Pistor and Mellado (2025). The study of de Lozar and Mellado (2017) revealed that additionally to the reduction of evaporation, a positive buoyancy flux is introduced through the sedimenting droplets, further reducing entrainment. Moreover, cloud droplet sedimentation acts on precipitation development, as shown by Wyant et al. (2007); Savic-Jovcic and Stevens (2008); Ackerman et al. (2009). They found that surface precipitation is reinforced in the presence of cloud droplet sedimentation, leading to an overall counteracting effect regarding the stratocumulus to cumulus transition: While droplet sedimentation reduces entrainment, impeding the SCT, it also enhances precipitation, that can cause an acceleration of the SCT.

Although there have been individual investigations with regards to both effects, to our knowledge, none of the previous studies considered the impact of cloud droplet sedimentation on stratocumulus in the context of the SCT. That is, all of the comparable studies targeting droplet sedimentation in subtropical stratocumuli simulate periods of at most six hours (Ackerman et al., 2004; Bretherton et al., 2007; Wyant et al., 2007; Ackerman et al., 2009; Hill et al., 2009; de Lozar and Mellado, 2017; Schulz and Mellado, 2019; Pistor and Mellado, 2025). Note that we do not include the 12 hour study by Igel (2024) here, as it focuses on the individual mechanisms instead of the combined effect on the cloud evolution. This implies that slower adjustments at the timescale of one day or more have not been examined. While six hours is enough for the initial stratocumulus evolution, it

https://doi.org/10.5194/egusphere-2026-479
Preprint. Discussion started: 29 January 2026

does not capture the deepening process until the breakup.

In this study, we address this gap by conducting 48 h long LES of 10 different cases, studying the impact of cloud droplet sedimentation on the pre-breakup stage of the SCT. Including multiple cases into our analysis is another novelty, as the aforementioned studies mostly focus on only one and at most up to three different cases. Here, we cover a variety of meteorological conditions of different seasons by selecting 10 transects from the Marine ARM GPCI Investigation of Clouds (MAGIC) ship campaign. The MAGIC campaign was executed in the Northeast Pacific from October 2012 until the end of September 2013 with a specific focus on the SCT. Hereby, the second ARM mobile facility was installed on the container ship Horizon *Spirit*, which conducted multiple transects between Los Angeles (California) and Honolulu (Hawaii). During these transects, comprehensive measurements of atmospheric, but also oceanic conditions like sea surface temperature were performed, that can serve as input for numerical simulations (Zhou et al., 2015).

Based on these observations, McGibbon and Bretherton (2017) demonstrated that modelling full MAGIC transects using high-resolution LES is possible in a ship-following frame of reference. Here, we employ a similar approach in order to simulate two full days covering the pre-breakup stage of the SCT. This paper is organised as follows: First, we describe the model characteristics and classify the chosen cases in Sect. 2. We then briefly evaluate two representative simulations in Sect. 3.1, after which the impact of sedimentation on the inversion height is discussed in Sect. 3.2. In Sect. 3.3, we propose a process chain to explain the observed behaviour and wrap up the analysis by presenting some sensitivity experiments in Sect. 4. Lastly, we summarise and contextualise our findings within the existing literature in Sect. 5.

2 Methodology

2.1 Simulation setup

In this study, we use the idealised single column mode (SCM) of the Icosahedral Nonhydrostatic (ICON) model (Zängl et al., 2015; Bašták Ďurán et al., 2021). The SCM is seamlessly integrated in the general ICON framework and can also be configured in a large-eddy simulation (LES) setup similar to Dipankar et al. (2015). This is achieved by using a model grid with multiple columns and enabling tracer transport as well as dynamics between the grid cells (e.g., Bašták Ďurán et al., 2022). To enable periodic boundary conditions, the simulations are run on a planar torus grid, which automatically connects the respective boundaries.

ICON uses a two-time level predictor-corrector scheme to integrate the dynamical core every dynamical time step, while diffusion, advection and the fast physics parametrisations are computed on a larger basic time step dt. Slow physics parametrisations as the ecRad radiation scheme by Hogan and Bozzo (2018) are called on a multiple of the basic time step. Sub-grid scale turbulence is modelled using the Smagorinsky-Lilly scheme (Smagorinsky, 1963; Lilly, 1962; Dipankar et al., 2015). Moreover, the two-moment bulk microphysics scheme by Seifert and Beheng (2006) without ice physics is employed, with some additions regarding droplet sedimentation as outlined in Sect. 2.2. Note that ICON uses a saturation adjustment instead of prognostic supersaturation.

https://doi.org/10.5194/egusphere-2026-479
Preprint. Discussion started: 29 January 2026

In our study, we run idealised simulations of 10 outbound MAGIC transects, called "A" legs. We simulate one control run (*control*) and one run with active droplet sedimentation parametrisation (*drop_sed*) for each leg for 48 h in an 8 km by 8 km domain with 50 m horizontal resolution. The vertical grid spacing is 9 m until 2.8 km, after which it is stretched to the model top at 20 km, with a total of 400 vertical levels. The first 6 h are disregarded as spinup with the exception of the analysis presented in Sect. 3.3, where the spinup period is shortened to 2 h.

Our setup closely follows that described in McGibbon and Bretherton (2017), so we will here only repeat important features or deviations. As the transect covers around 2000 km, high-resolution simulations are only feasible in a ship-following configuration, that is, the geographical location of the small domain needs to follow the ship track. The original ICON-SCM version lacked this feature, so it was added manually. The simulations are initialised using the first applicable ship-launched sounding and forced using geostrophic winds, ship-following advective tendencies for temperature and humidity and the large-scale vertical velocity. Furthermore, the sea surface temperature is prescribed and used to compute the surface fluxes in a version of the Louis (1979) parametrisation. On top of that, we employ the same relaxation strategy as McGibbon and Bretherton (2017). We nudge the horizontal mean wind towards the observed sounding wind every 12 hours, whereas we nudge humidity and temperature every 30 min, but only from 3 km upwards. In addition, McGibbon and Bretherton (2017) prescribed the cloud droplet number concentration N_d based on ship measurements of cloud condensation nuclei (CCN), which is not possible in a two-moment microphysics scheme, as both mass and number concentrations are predicted. Instead, in ICON's two-moment scheme, a uniform background CCN concentration is prescribed below 4 km, which decays exponentially above this threshold. We choose the pre-existing intermediate concentration of $250\,\mathrm{cm}^{-3}$ for all legs to simplify the analysis, but conduct a sensitivity experiment addressing this choice in Sect. 4.3.

2.2 Cloud droplet sedimentation

The original ICON two-moment microphysics scheme does not contain the process of sedimenting cloud droplets due to their low sedimentation velocity. However, as all spherical hydrometeors are treated in the same way, cloud droplet sedimentation can be added conveniently. As Seifert and Beheng (2006) is a standard microphysics scheme, we only present a brief overview of the necessary equations for sedimentation and refer to the paper for details.

Hydrometeor masses x are assumed to follow the generalised Γ-distribution

$$f(x) = A\,x^{\nu}\exp(-\lambda x^{\mu})\,, \tag{1}$$

where $A = A(N, L)$ and $\lambda = \lambda(N, L)$ are moment-dependent parameters (cf. Eq. (80) of Seifert and Beheng, 2006) and μ, ν are hydrometeor-specific shape parameters. In a two-moment scheme, the zeroth moment N, i.e. the number density, as well as the first moment L, i.e. the mass density, are predicted. Sedimentation is addressed by solving the partial differential equation

$$\frac{\partial m}{\partial t} = -\frac{\partial}{\partial z}\left(\bar{v}_m \cdot m\right) \tag{2}$$

with the mean sedimentation velocity $\bar{v}_m$ for each moment $m = \{N, L\}$ and species individually. The bulk sedimentation velocity $\bar{v}_m$ can be obtained by computing the respective velocity-weighted moment using the individual fall velocity $v(x)$.

https://doi.org/10.5194/egusphere-2026-479
Preprint. Discussion started: 29 January 2026

Apart from rain, the latter are assumed to follow a power-law relationship

$$v(x) \simeq \alpha x^{\beta} \left(\frac{\rho_0}{\rho}\right)^{\gamma}, \tag{3}$$

with $\rho_0 = 1.225\,\mathrm{kg\,m^{-3}}$, hydrometeor-specific constants α, β, γ and a density correction $\sim \rho^{-1}$ to account for the change in atmospheric density. For cloud droplets, $\alpha = 3.75 \cdot 10^{-5}\,\mathrm{m\,s^{-1}kg^{-\beta}}$, $\beta = 2/3$ and $\gamma = 0.2$, where the density correction exponent γ is smaller than the original $\gamma = 0.4$ for the other hydrometeors due to the considerably lower mass.

The ICON two-moment microphysics offers two options to calculate hydrometeor sedimentation, a semi-implicit approach and an explicit approach. Apart from the different numerical implementations, which we will not discuss here, the main physical difference between them stems from the calculation of the sedimentation flux. In the semi-implicit scheme, the sedimentation flux is calculated by taking into account the updated inflow from all overlying levels within the current time step. By contrast, the explicit scheme only considers the state from the previous time step and does not account for the inflow from above (A. Seifert, 2024, pers. comm.). In the present study, we opted for the explicit approach, as the impact of including inflow from the current time step is very limited. Even for heavy rainfall, which is not likely to occur in marine stratocumulus, a terminal velocity of $v_{\max} = 10\,\mathrm{m\,s^{-1}}$ (Pruppacher and Klett, 1997) would lead to a Courant number of

$$C = \frac{v_{\max} \cdot dt}{\Delta z} \approx 0.56 \tag{4}$$

with our settings $dt = 0.5\,\mathrm{s}$ and $\Delta z = 9\,\mathrm{m}$, implying that even fast settling rain would not be able to reach the next grid box. For more technical details on the numerical implementation of the explicit scheme, we refer to Blahak (2020); Bolt and Omanovic (2026).

2.3 WTG correction

In order to keep the simulated inversion height close to the observed one over the course of multiple days, McGibbon and Bretherton (2017) employed a weak temperature gradient (WTG) correction based on Blossey et al. (2009). In the WTG framework, it is assumed that horizontal temperature gradients in the free troposphere are small. Thus, temperature perturbations can be connected directly to vertical motion in the atmospheric column. Blossey et al. (2009) achieved this through a damped gravity wave approach. Treating the observed temperature as the reference profile, it is possible to calculate a correction to the vertical velocity ω in pressure coordinates using the partial differential equation:

$$\frac{\partial}{\partial p}\left(\frac{f^2 + a_m^2}{a_m}\frac{\partial \omega'}{\partial p}\right) = \frac{k^2 R_d T_v'}{p}. \tag{5}$$

Here, T_v' is the deviation of the virtual temperature from the reference profile, R_d is the dry gas constant, $k = 2.4 \cdot 10^{-6}\,\mathrm{m^{-1}}$ is the wavenumber of the gravity wave, f is the Coriolis parameter and $a_m = 1\,\mathrm{d^{-1}}\, p\,(1000\,\mathrm{hPa})^{-1}$ is the momentum damping rate. The reference virtual temperature is computed from the large-scale forcings. Furthermore, it is assumed that ω vanishes at the surface and the tropopause (Blossey et al., 2009). This yields a correction term that acts to lower (raise) the LES inversion through increased (decreased) subsidence, in case it starts to drift upwards (downwards).

https://doi.org/10.5194/egusphere-2026-479
Preprint. Discussion started: 29 January 2026

In the setup of McGibbon and Bretherton (2017), this correction was calculated during the simulations to adjust the vertical velocity dynamically. We cannot adopt this procedure in our study, since we want to compare the outcome of *control* and *drop_sed* targeting the cloud droplet sedimentation mechanism. Applying a dynamical correction would distort the sedimentation effect, as in both cases the simulations would be drawn to the reference profiles. To nevertheless obtain results, that qualitatively fit to the observations, we opt for an offline WTG correction. We conduct *control* runs for each leg with the original large-scale vertical velocity in a low resolution setup on a $4\,\mathrm{km}$ by $4\,\mathrm{km}$ domain with around $132\,\mathrm{m}$ horizontal resolution. Moreover, we only use 200 vertical levels with a layer thickness of at most $25\,\mathrm{m}$ below $3\,\mathrm{km}$ and stretched above. Lastly, we strictly nudge the simulation state to the reference temperature and humidity above $3\,\mathrm{km}$ on a timescale of $1\,\mathrm{min}$ to ensure that reference and simulation are correctly synced above the boundary layer. Note that this coarser setup produces results that are qualitatively similar to those obtained at finer resolution.

Then, we compute the WTG correction offline based on Eq. (5), add it to the original vertical velocity and perform a first iteration *control* run. Clearly, this approach is not optimal, as the offline WTG computation does not take into account the induced changes from previous time steps and therefore tends to overcorrect in the later stages. To account for this overcorrection, we compute the offline WTG correction for this first iteration run, perform a second iteration run, compare the outcomes and take the best fit iteration (i.e. first or second iteration) based on the development of the inversion height. This approach yields a consistent outcome for all cases, exhibiting the characteristic deepening and the sub-cloud layer cumulus evolution, which is the main point of interest in our study (cf. Fig. A1). The individual choices for the WTG iterations can be found in Table 1.

2.4 Case classification

Before we present the results, we provide a short overview of the individual legs, collected in Table 1. As aforementioned, our study contains cases from all seasons including a variety of meteorological conditions. The broad majority of transects was executed in warmer months, where the large lower tropospheric stability leads to a stable situation, in which stratocumulus decks can readily form under a strong inversion (Klein and Hartmann, 1993; Wood, 2012). The third column demonstrates that while most of the cases begin close to the North American coast, three start further offshore than $126^\circ\,\mathrm{W}$ (or $800\,\mathrm{km}$). Note that the distance in km is the great-circle distance from Los Angeles (LA), which was computed based on the ship's geographical position, and is a solid approximation of the ship's path (Zhou et al., 2015).

In the subsequent analysis, if not stated otherwise, we focus on the stratiform stages where a domain-averaged cloud fraction f_c of at least $40\,\%$ exists. We chose this particular threshold to eliminate periods of non-existing stratocumulus decks as well as to cut legs that have already completed the transition and have broken up irreversibly. On the grid-scale, f_c is binary with either $100\,\%$ or $0\,\%$, which is determined by a cloud water mixing ratio threshold of $10^{-8}\,\mathrm{kg\,kg^{-1}}$. Note that the cloud water hydrometeors and the rain water hydrometeors in ICON are separated by a mass threshold of $x^* = 2.6 \cdot 10^{-10}\,\mathrm{kg}$. In this study, liquid water content q_c, liquid water path (LWP) and the subscript c refer to cloud water, whereas rain water path (RWP) and the subscript r refer to rain water, unless stated otherwise. The final location of the stratocumulus deck in the *control* runs can be found in the fourth column of Table 1, where legs that transitioned before the end of the simulation are highlighted in red.

https://doi.org/10.5194/egusphere-2026-479
Preprint. Discussion started: 29 January 2026

Table 1. Summarised information about the simulated MAGIC legs: The leg numbers, the simulation starting time, the ship's location at the starting time, the final location of the stratocumulus period in the *control* run depending on whether the simulation ended before the breakup or the cloud deck broke up midway (red), the season of the transect, the number of WTG iterations performed, the domain-averaged maximum liquid water path (LWP) of the first 6 h of the *control* run with a horizontal mean cloud fraction of at least 40 %, as well as the resulting optical thickness classification. The locations are given in both longitude and distance from Los Angeles.

leg	starting time (UTC)	starting location [° W]	([km])	stratocumulus end [° W]	([km])	season	WTG iteration	LWP [g m^{-2}]	longwave emissivity
04A	2012-10-20, 18:00	120.2	(227)	137.4	(1958)	autumn	second	13	unsaturated
05A	2012-11-04, 00:00	120.1	(202)	137.6	(1910)	autumn	second	124	saturated
07A	2012-12-01, 17:30	119.2	(125)	131.9	(1387)	winter	first	85	saturated
11A	2013-05-13, 18:00	129.0	(1091)	146.0	(2861)	spring	first	28	unsaturated
12A	2013-06-09, 17:15	128.8	(1077)	145.8	(2839)	summer	second	145	saturated
13A	2013-06-22, 17:45	119.7	(198)	133.2	(1482)	summer	second	130	saturated
14A	2013-07-08, 05:30	122.1	(405)	136.9	(1902)	summer	second	140	saturated
15A	2013-07-20, 17:30	119.7	(179)	137.2	(1932)	summer	second	123	saturated
16A	2013-08-03, 23:30	121.6	(354)	138.2	(2043)	summer	first	123	saturated
17A	2013-08-18, 17:45	126.3	(827)	135.4	(1749)	summer	first	82	saturated

As the f_c threshold is applied for each leg individually, this can yield small time periods where one run is still in a stratiform stage, while the other is not. To make the analysis more comparable, we use the more conservative outcome for both runs, as these events occur only infrequently.

We divide all 10 cases into two categories: saturated and unsaturated. This classification is based on the amount of liquid water in the cloud deck and targets the blackbody behaviour of a cloud regarding its longwave emissivity. It is well-known that a cloud's longwave emissivity (and thus, its integrated radiative cooling) is approximately constant at LWP $\gtrsim 30-50\,\mathrm{g\,m^{-2}}$ (e.g. Stephens, 1978; Turner et al., 2007; Williams and Igel, 2021). However, at lower values, this emissivity increases with LWP and so does the radiative cooling that drives stratocumulus development. As summarised in the last two columns, eight legs fall in the saturated category, while two belong to unsaturated with domain-averaged maximum LWP well below $50\,\mathrm{g\,m^{-2}}$ in the first 6 h. Note here, that rain water contributes to longwave emissivity in principle, however, its impact is negligible during the early stages of the unsaturated legs (e.g. Fig. 3). For consistency, Table 1 therefore reports LWP only, as including rain water would not affect the outcome.

https://doi.org/10.5194/egusphere-2026-479
Preprint. Discussion started: 29 January 2026

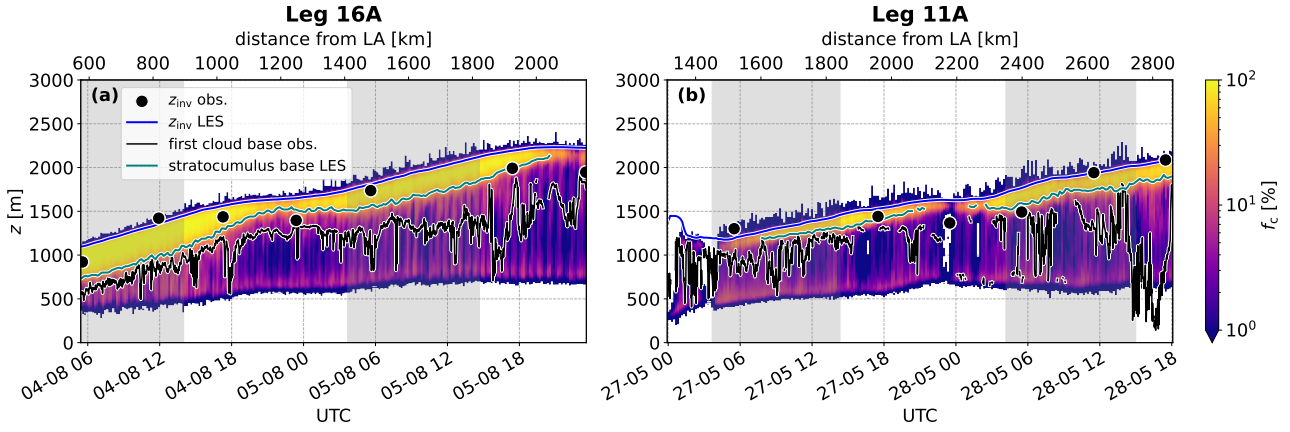

Figure 1. Domain-averaged cloud fraction f_c of the *control* runs of **(a)** Leg 16A and **(b)** Leg 11A as a function of height z over the course of the simulation. The bottom x-axis marks the respective time of the transect, while the top x-axis marks the distance from Los Angeles. The blue line shows the LES inversion, while the teal line shows the lowest height of $f_c = 40\,\%$, if it exists. The black dots symbolise the observed inversion height based on the ship radiosonde launches (Keeler et al.), whereas the black line depicts the observed first cloud base based on the ship ceilometer (Zhang et al.). The latter was resampled to a time step of 1 min for better visibility. Grey shading marks local night-time.

3 Results

3.1 Qualitative evaluation of the deepening evolution

Before we focus on the impact of cloud droplet sedimentation, we will briefly evaluate the quality of our simulations. In doing so, we first compare *control* runs of two representative legs of each category to MAGIC ship observations regarding inversion height and cloud base height, and assess the overall development of the SCT. The simulated inversion height z_{inv} in this study is determined by the height of maximum gradient of liquid water potential temperature θ_l in the boundary layer. It is computed at each time step and each grid cell and averaged over the domain afterwards. The observed inversion height is computed using profiles of potential temperature θ instead of θ_l, as no condensate was measured in the regular ship radiosonde launches.

Figure 1 depicts the evolution of the domain-mean f_c of the saturated Leg 16A as well as the unsaturated Leg 11A, excluding the 6 h spinup window. The expected course of the SCT is nicely visible for the saturated leg in panel (a). Starting with a low-lying thick stratocumulus deck of high f_c, z_{inv} increases continuously, until cloud breakup occurs in the very end. During this process, the stratocumulus deck decouples from the surface and cumulus clouds form below the main deck, indicated by a low f_c below the stratiform cloud deck. This behaviour is consistent with the initial stages of the deepening-warming mechanism by Bretherton and Wyant (1997); Wyant et al. (1997), where the rise in sea surface temperature drives decoupling from the surface. Analogous simulation results for the initial stages of the SCT in MAGIC transects could be obtained by McGibbon and Bretherton (2017); Zheng et al. (2020). The influence of the diurnal cycle is also identifiable, with episodes of continuous

https://doi.org/10.5194/egusphere-2026-479
Preprint. Discussion started: 29 January 2026

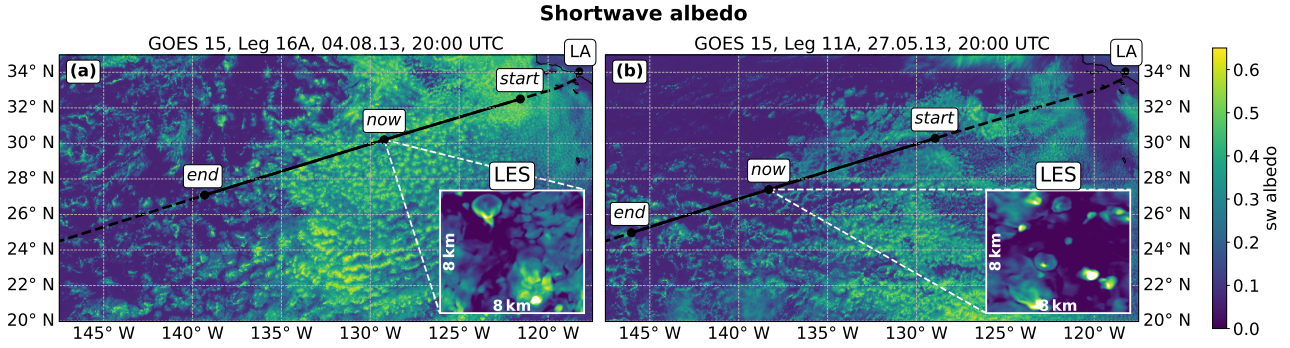

Figure 2. GOES 15 broadband shortwave (sw) albedo snapshot of **(a)** Leg 16A and **(b)** Leg 11A around midday of the respective day. The dashed black line shows the full MAGIC transect starting from the Los Angeles harbour, while the solid black line shows the simulated part (enclosed by *start* and *end*). The midpoint (*now*) indicates the ship's position during the snapshot. For comparison, the LES pseudo-albedo of this time step is depicted in the small rectangle.

cloud thickening and inversion rise during night-times in contrast to cloud thinning and inhibited growth during day-times during solar insolation. The LES inversion tracks the observed inversion quite well, apart from a bias during day-times, where the inversion seems to decline in the observations. Moreover, the observed first cloud base from the ship ceilometer (hereafter cloud base) follows the stratocumulus base relatively steadily in the beginning. Afterwards, it starts oscillating between the stratocumulus base and the underlying cumuli, depending on whether the ship passes under a cumulus cloud or only the stratocumulus deck. Overall, the vertical extension and location of the cloudy layer as a whole is captured well.

In panel (b), the unsaturated Leg 11A is depicted. It is noticeable that the cloud deck is absent at first, forming during the first night. The simulated transect begins more than $1000\,\mathrm{km}$ off the coast, leading to an immediately (semi-) decoupled stratocumulus deck with underlying cumuli. The second obvious difference to Leg 16A is the thickness of the deck accompanied by a brief day-time breakup in the middle of the transect. Apart from that, both the deepening process and the diurnal cycle are similar. Furthermore, the observed inversion as well as the observed cloud base exhibit the same features as in panel (a). They are tracked quite well by the simulated cloud, apart from the day-time bias of the inversion. The cloud base also shows brief disruption episodes, pointing at the structure of a thinner, more broken-up stratocumulus deck. At the end of the second night, the observed cloud base drops abruptly to around $200\,\mathrm{m}$, which is not reproduced by the LES. In total, our simulations successfully capture the initial SCT development regarding the deepening of the boundary layer as well as the decoupling from the surface together with the formation of underlying cumuli.

Secondly, we want to evaluate the simulations by comparing them to satellite observations. Figure 2 depicts the domain albedo for the same two representative legs, 16A for saturated and 11A for unsaturated. The background plot shows a midday snapshot of the broadband shortwave albedo from the Fifteenth Geostationary Operational Environmental Satellite (GOES 15), obtained using the techniques described in Minnis et al. (2002, 2008, 2011) at a pixel resolution of $4\,\mathrm{km}$. The image during Leg 16A in

https://doi.org/10.5194/egusphere-2026-479
Preprint. Discussion started: 29 January 2026

panel **(a)** represents a prime example of a subtropical SCT. It is characterised by an extensive, contiguous stratocumulus deck of high albedo, that starts to break up at around $134^\circ\,\mathrm{W}$ and transitions into free ocean cumuli. In contrast, the cloud deck during Leg 11A in panel **(b)** is more fragmented, has lower albedo and breaks up earlier. The small embedded rectangle shows the LES pseudo-albedo α of the $8\,\mathrm{km}$ by $8\,\mathrm{km}$ domain at the time of satellite snapshot, which serves as a proxy for the real albedo. We use the approach outlined in Dhandapani et al. (2025) and calculate α following Szczap et al. (2014):

$$\alpha = \frac{(1-g)\,\tau}{2+(1-g)\,\tau}\,. \tag{6}$$

Hereby, $g = 0.86$ is the asymmetry factor and τ is the optical depth calculated after Stephens (1978) by

$$\tau = \sum_{i=\mathrm{c,r}} \frac{3}{2} \int \frac{q_i(z)\,\rho(z)}{r_{\mathrm{eff},i}(z)\,\rho_\mathrm{w}}\,dz\,, \tag{7}$$

summing over the individual contributions of cloud and rain water. ρ represents the local air density, $\rho_\mathrm{w} = 1000\,\mathrm{kg\,m^{-3}}$ represents the density of water, r_eff and q denote the effective radius and the mixing ratio of the respective liquid hydrometeor. The magnitude of the pseudo-albedo largely matches the satellite in both cases. Similarly, both simulation domains capture the differences in cloud morphology between the two cases described above. The saturated Leg 16A case exhibits a broad cloud deck covering most of the LES domain, whereas Leg 11A is far less extensive and features more isolated cumuli, consistent with conditions in the breakup region. In both cases peak albedos inside individual cumuli exceed observed albedo ranges. Furthermore, the simulated cloud deck during Leg 16A seems to be a little more broken than observed. However, it is important to be aware of the scales. The LES domain corresponds to only two by two pixels in the satellite image. Overall, it is encouraging that the individual simulations exhibit analogous differences to those shown in the satellite images.

3.2 The impact on the inversion height

A common measure for analysing boundary layer growth is the entrainment velocity

$$w_\mathrm{e} = \frac{\mathrm{d}z_\mathrm{inv}}{\mathrm{d}t} - w_\mathrm{sub,inv}\,, \tag{8}$$

originally introduced by Lilly (1968). The calculation involves the change in z_inv and the subsidence velocity w_sub at the inversion. In the following, we decide against the usage of w_e in illustrating plots and instead discuss z_inv directly. The reason is that w_e oscillates considerably due to the temporal derivative, requiring substantial smoothing to become interpretable, whereas z_inv itself is smooth. However, we continue to use the exact w_e when comparing changes with values reported in the literature, in order to enable a quantitative evaluation. Qualitatively, variations in z_inv mirror those in w_e, as deviations in the subsidence velocity at the inversion are small between *drop_sed* and *control* for the majority of the time, and thus

$$w_\mathrm{e,\,drop\_sed} - w_\mathrm{e,\,control} = \Delta w_\mathrm{e} \approx \Delta\left(\frac{\mathrm{d}z_\mathrm{inv}}{\mathrm{d}t}\right) \tag{9}$$

holds. In the following, all differences Δ are computed as *drop_sed - control*.

To enable a more compact analysis, we distribute the legs in the two categories as in Table 1. While the unsaturated category

https://doi.org/10.5194/egusphere-2026-479
Preprint. Discussion started: 29 January 2026

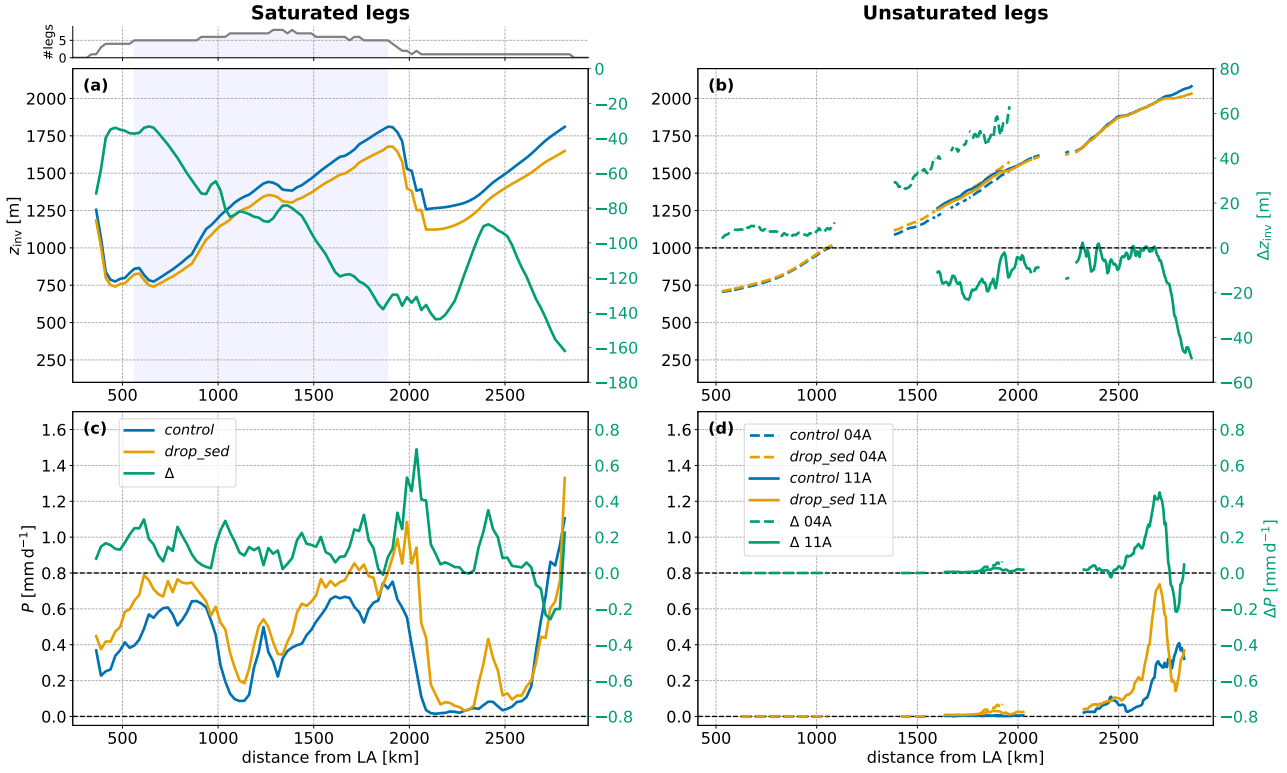

Figure 3. Binned distance plots of the inversion height z_{inv} (top panels) and the precipitation rate P (bottom panels), separated by category. Panels **(a)** and **(c)** represent the saturated legs, whereas panels **(b)** and **(d)** represent the unsaturated legs. The former are combined into one curve with the leg contribution depicted above the panels in grey, whereas the latter are depicted individually using dashed (solid) lines for Leg 04A (Leg 11A). The left y-axis corresponds to the absolute magnitude of both *control* (blue) and *drop_sed* (orange), while the right y-axis corresponds to the difference Δ (green). The light blue shading indicates the core region, where at least five legs are contributing. In all panels save for **(b)**, a rolling mean of roughly $75\,\mathrm{km}$ was applied.

only consists of two legs, the saturated one contains eight legs, complicating an individual assessment. Due to their similar behaviour, we opt for a composite analysis in the latter. We use the great-circle distance to Los Angeles for each leg, bin the data in $25\,\mathrm{km}$ intervals and then average over all legs in the category in order to acquire one distance-binned dataset. Obviously, the physical interpretation has changed in this setup, as this results in average quantities of all respective transects. However, for our purpose, this is the preferred outcome, since we aim to compare *drop_sed* and *control*, which consist of the same transects. Thus, in the subsequent analysis, we deal with averaged quantities in the saturated category, while we stick to the two unsaturated legs individually, as also their distance overlap is small.

The top panels of Fig. 3 show the development of z_{inv} in both categories. In panel (a), the averaged inversion of the eight saturated legs follows the expected continuous increase in the direction of the free ocean. However, there are two sharp drops,

https://doi.org/10.5194/egusphere-2026-479
Preprint. Discussion started: 29 January 2026

one in the beginning and another at around $2000\,\mathrm{km}$. Both can be explained by the number of legs contributing to these intervals. The former originates from Leg 07A, being the only leg this close to the coast, but having a relatively high stratocumulus deck, while the latter comes from Leg 12A, which starts very late compared to all other thick legs and has a strong low-lying deck (see Fig. A1). Δz_{inv} is becoming more negative, apart from the very beginning and a considerable period around $2300\,\mathrm{km}$, indicating reduced entrainment in the *drop_sed* runs. While the initial increase is an artifact of the averaging procedure, when new legs are added (cf. the distribution above panel (a)), the sharp increase in the later stage is a distinct feature of Leg 12A, which will be discussed in Sect. 4.1. The increasing negative divergence in the core region between $550\,\mathrm{km}$ and $1900\,\mathrm{km}$ (indicated by the blue shading) corresponds to a mean reduction in w_{e} of around $9\,\%$, which is in good agreement with previous studies. The non-precipitating LES studies of Bretherton et al. (2007); Hill et al. (2009) yielded a reduction in w_{e} of around $7\,\%$, while Ackerman et al. (2009) reported a decrease of up to $25\,\%$ in their precipitating case. de Lozar and Mellado (2017); Pistor and Mellado (2025) found even stronger reductions of $20\,\%$ to $50\,\%$ in their DNS, as these simulations generally observe more pronounced effects through their fine resolutions. It is important to acknowledge that the present value of $9\,\%$ is an average over different transects and also includes diurnal cycle effects, while the other LES studies consist of one specific case in nocturnal conditions. Here, we observe individual periods of reduced entrainment that can be as large as $20\,\%$ in precipitating cases, consistent with Ackerman et al. (2009).

In contrast, the unsaturated cases in panel (b) show a different behaviour. While the development of the deepening boundary layer is the same for both Leg 04A (solid) and Leg 11A (dashed), the behaviour of *control* compared to *drop_sed* differs crucially. For Leg 04A, Δz_{inv} is constantly increasing after $1000\,\mathrm{km}$, implying that entrainment is enhanced in the *drop_sed* run. In this case, this even leads to a $60\,\mathrm{m}$ deeper boundary layer at the end of the simulation. In this period, a mean entrainment amplification of $10\,\%$ is observed, which is of comparable magnitude to the previously reported reductions in LES studies. For Leg 11A, this effect is not as pronounced, but still noticeable. The inversion in the *drop_sed* run starts roughly $10\,\mathrm{m}$ below the *control* one after the delayed cloud formation (cf. Fig. 1, panel (b)). After a brief increase of this deviation, the trend is a slow, but steady decrease, which can be quantified to a mean entrainment amplification of $2\,\%$ in the *drop_sed* case. As soon as Δz_{inv} reaches $0\,\mathrm{m}$, an abrupt drop occurs, that can be attributed to the sudden formation of drizzle (cf. panel (d), details in Sect. 4.2). To our knowledge, enhancement of entrainment in stratocumulus due to cloud droplet sedimentation has not been reported before.

The bottom panels of Fig. 3 depict the corresponding precipitation rates in both categories. The saturated cases in panel (c) develop relatively strong precipitation throughout the majority of the transects, which is comparable to the heavy drizzle rates of $1\,\mathrm{mm\,d^{-1}}$ in Stevens et al. (1998); Savic-Jovcic and Stevens (2008). The reason for the seemingly lower values and the oscillatory behaviour is the averaging over multiple legs, leading to a mix of day-time and night-time. It is evident that the precipitation rates are considerably increased in the presence of droplet sedimentation, in accordance with Ackerman et al. (2009). In contrast, the precipitation rates of the unsaturated cases in panel (d) are very small. Leg 04A develops almost no surface precipitation at all, independent of the type of simulation. Leg 11A also shows very limited precipitation, apart from the final stage of the simulation, where a sharp enhancement can be observed. This increase is greatly reinforced in the *drop_sed*

https://doi.org/10.5194/egusphere-2026-479
Preprint. Discussion started: 29 January 2026

Table 2. Leg-wise mean quantities of the first 3 h after cloud formation, excluding 2 h of spinup. The first row shows the inversion height z_{inv}, whereas the second row shows the mean cloud-top height z_{ct}, with the results for the spinup experiment of Leg 04A in grey. The third (fifth) and fourth (sixth) row represent the liquid (rain) water path (LWP; RWP) and its difference Δ, respectively, while the last row lists the sedimentation velocity $v_{\mathrm{sed},75}$ of the *drop_sed* run in the 75 m below z_{inv}. Recall that $\Delta x = x_{\mathrm{drop\_sed}} - x_{\mathrm{control}}$ for all variables x.

leg	04A	05A	07A	11A	12A	13A	14A	15A	16A	17A
Δz_{inv} [m]	-3.2 (-1.9)	-3.8	-48.6	-14.2	10.7	-8.3	-5.8	-5.4	-7.5	-19.8
Δz_{ct} [m]	-5.5 (-3.7)	-5.4	-52.0	-22.2	-15.3	-15.7	-7.4	-11.7	-11.2	-25.2
$\mathrm{LWP}_{\mathrm{control}}$ [$\mathrm{g\,m^{-2}}$]	10.5	13.6	94.0	13.9	100.5	129.8	79.4	54.3	105.5	108.0
$\Delta\mathrm{LWP}$ [$\mathrm{g\,m^{-2}}$]	2.3	1.1	-0.2	1.2	-15.8	3.7	0.6	4.2	-5.1	-13.9
$\mathrm{RWP}_{\mathrm{control}}$ [$\mathrm{g\,m^{-2}}$]	$9.3 \cdot 10^{-3}$	$2.6 \cdot 10^{-3}$	9.2	0.2	1.5	6.0	0.3	0.2	6.3	6.7
$\Delta\mathrm{RWP}$ [$\mathrm{g\,m^{-2}}$]	$1.5 \cdot 10^{-2}$	$1.6 \cdot 10^{-3}$	2.7	0.3	2.9	1.5	1.5	1.2	6.9	7.8
$v_{\mathrm{sed},75}$ [$\mathrm{cm\,s^{-1}}$]	0.65	1.06	1.77	0.48	2.27	2.25	2.10	1.66	1.91	1.89

case, directly affecting z_{inv} in panel (b). From that, we can conclude that precipitation is a strong factor in the boundary layer development of the present cases.

3.3 The turbulence feedback mechanism

The observations from the previous section raise two main questions. First, how can droplet sedimentation lead to enhanced entrainment and second, why does this predominantly occur in the unsaturated legs. In this section we aim to disentangle the primary process chain by examining the temporal evolution of the sedimentation effect in two stages: the short-term effect in the initial hours and the long-term effect afterwards.

Sedimentation acts to remove cloud water from the cloud-top layer and thereby reduces evaporation. This reduction in evaporation impedes entrainment and directly leads to an increase in LWP, as found by Bretherton et al. (2007); Wyant et al. (2007); Ackerman et al. (2009); Pistor and Mellado (2025). The initial reduction in entrainment is visible in all our simulations, not only the saturated ones, but also the unsaturated ones. To quantify this, we computed the mean Δz_{inv} in the hours 2 to 5 for each leg, except Leg 11A, where we used the hours 13 to 16 due to the delayed cloud formation. This way, we discard only the two initial hours as spinup, after which the simulations have mostly stabilised. For Leg 04A, the reduction occurs mainly in the first 4 h, which is not displayed in Fig. 3 due to the discarded spinup window of 6 h. To verify that the observed effect is not an artifact of model spinup, we conduct another simulation for this leg. In doing so, we start with the *control* settings, but activate droplet sedimentation after 15 h and let the simulation evolve until the end. We chose this particular activation time step, as the cloud deck's properties such as thickness or LWP, are comparable to the initial hours. A plot for the resulting z_{inv} for Leg 04A can be found in the appendix Fig. A2.

The results for all legs are summarised in Table 2 with the sensitivity result for Leg 04A in grey brackets. The first two rows

https://doi.org/10.5194/egusphere-2026-479
Preprint. Discussion started: 29 January 2026

present the difference of two measures for the stratocumulus top: z_{inv} and the mean cloud-top height z_{ct}. The latter is calculated from the maximum height of the cloud water mixing ratio $> 0.01\,\mathrm{g\,kg^{-1}}$ in each column (Ackerman et al., 2009) and is averaged over the domain afterwards. It serves as an additional tool to check if z_{inv} behaves as expected in the initial hours of the simulation. Note that Δz_{ct} evidently leads to larger differences than Δz_{inv}, as it is directly driven by the sedimenting droplets. Both approaches yield an overall negative difference for all legs, apart from Leg 12A (marked in red), confirming the reduced entrainment in the initial hours. For Leg 12A, only z_{ct} confirms the reduced entrainment, whereas z_{inv} disagrees. However, in this case, the thermodynamic inversion clearly does not fit to the top of the cloud in the early hours of the simulation (cf. Fig. A3), which is further indicated by its actual high sedimentation velocity. Considering this, we conclude that also in this case, entrainment is indeed reduced in the initial hours.

Regarding the sedimentation velocity, it is clear that legs with a low initial LWP also have substantially lower sedimentation velocities due to their smaller effective radii. Comparing $\mathrm{LWP_{control}}$ to the mean LWP in Table 1, it is noticeable that some of the saturated legs (especially Leg 05A and Leg 15A) would be categorised as unsaturated. However, this is simply an artifact of the initial cloud formation, that vanishes shortly. The expected increase in LWP in the *drop_sed* runs (i.e. positive ΔLWP values in the fourth row) is not observed uniformly for all legs. Instead, a decrease is observed for the legs 07A, 12A, 16A and 17A. However, taking into account the change in RWP in the sixth row, this deviation can be readily explained by the considerable amplification of rain water in these cases. The excess is at least $2.7\,\mathrm{g\,m^{-2}}$, while the other legs have a maximum excess of $1.5\,\mathrm{g\,m^{-2}}$. The rain water depletes the cloud by collecting droplets and removes them through precipitation, which is enhanced in *drop_sed* by the sedimenting cloud droplets (Ackerman et al., 2009). In the other cases, this enhancement does not (yet) dominate and thus, the reduction in entrainment yields an increase in LWP.

So far, we have seen that the initial stages indeed yield the expected reduction in entrainment accompanied by an increase in LWP, if the simultaneous increase in RWP is not too strong. Rain formation in general is obviously crucial, as drizzle in stratocumulus can have a substantial effect on boundary layer dynamics by, among other things, depleting the cloud of liquid water or reducing turbulent kinetic energy (TKE) (e.g., Stevens et al., 1998; Savic-Jovcic and Stevens, 2008). For now, we will restrict our analysis to the general cases, but we will treat the impact of precipitation in a sensitivity experiment in Sect. 4.2.

Next, we focus on the impact of sedimentation after the initial period, continuing with the amount of liquid water in the cloud. Figure 4 shows the mean relative q_{c} profile, as well as the mean relative radiative heating rate profile, split up into the two categories. These profiles (and all subsequent ones) were obtained as follows: For each leg at each time step after the $6\,\mathrm{h}$ of spinup, the height coordinate was normalised by the corresponding z_{inv}. After that, the corresponding legs were merged and a normalised mean profile over all time steps was computed in both categories. Starting with the saturated legs, the decline in LWP, which was already foreshadowed in Table 2, is also visible in the overall mean in panel (a). The stratocumulus region around the maximum of the profile shows a clear decrease, while there is a slight increase in the sub-cloud areas in the *drop_sed* runs. Moreover, the maximum also dropped considerably due to the sedimenting droplets. In contrast, the unsaturated legs retain and even amplify their initial liquid water increase throughout the entire cloud layer. One reason behind that is the lack of drizzle in the unsaturated cases, which only only forms towards the end of the simulation in both legs (cf. Fig. 3,

https://doi.org/10.5194/egusphere-2026-479
Preprint. Discussion started: 29 January 2026

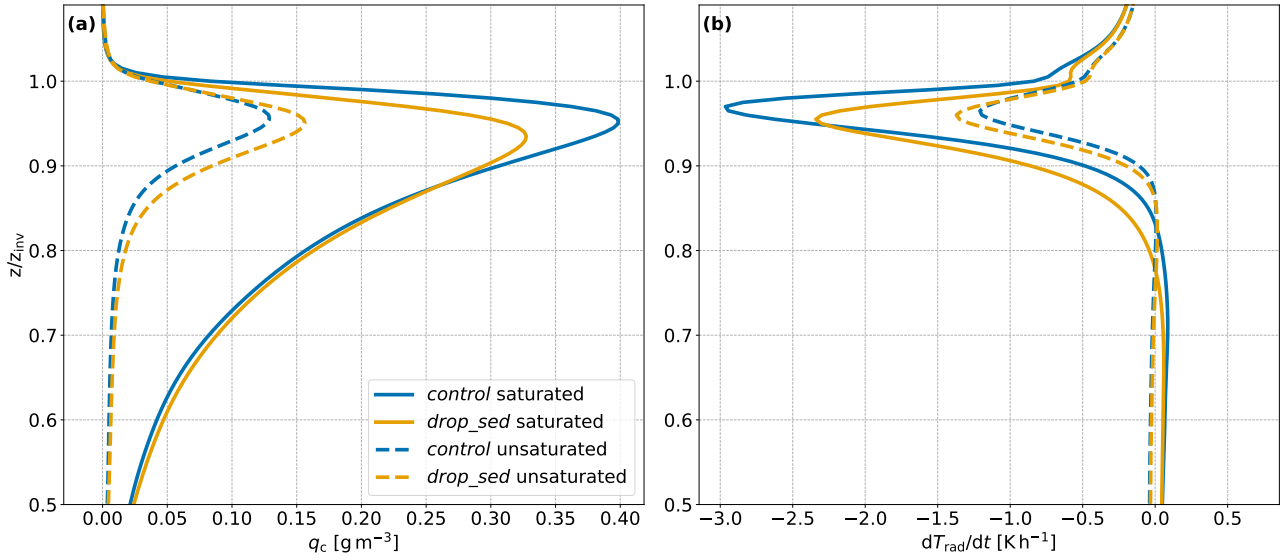

Figure 4. Total mean relative profiles of **(a)** liquid water content q_c and **(b)** radiative heating rate $\mathrm{d}T_{\mathrm{rad}}/\mathrm{d}t$. The profiles were normalised to the inversion height z_{inv} at each time step before computing the mean. The saturated (unsaturated) legs are represented by solid (dashed) lines. Note that the y-axis is cut at 0.5. Colours as in Fig. 3.

panel(d)), and thus, does not drain the cloud of liquid water.

This behaviour is also reflected in the radiative heating rate in panel (b). The peaks in both *drop_sed* curves have shifted to lower relative heights. In the saturated cases, the peak cooling rate declined substantially. However, most of it was simply transferred to lower heights, where a comparable strengthening can be observed. In contrast, the unsaturated cases show an amplification in longwave cooling across the full cloud layer, consistent with the q_c profile in panel (a). The reason for the overall increase, instead of a shift as for the saturated legs, is the LWP dependence of the longwave cooling, which was the mean criterion for our categorisation in Sect. 2.4. For the unsaturated legs, an enhancement in LWP still leads to an enhancement in integrated longwave cooling, which is why the cooling rate is amplified across the entire layer (Stephens, 1978; Turner et al., 2007).

Figure 5 presents analogous profiles of selected turbulence quantities. In the unsaturated case, the overall increased q_c, combined with enhanced longwave cooling, is expected to amplify turbulent circulations in the boundary layer (e.g. Feingold et al., 2015). Panel (a) shows the buoyancy flux, which is indeed enhanced in the *drop_sed* case throughout the cloud layer, while it remains relatively unchanged below. In contrast, the saturated legs exhibit the opposite behaviour. Buoyancy production is considerably decreased in the upper cloud layer and relatively constant elsewhere, apart from an increase near the surface. The former decrease can be attributed to several stabilising factors. The removal of liquid water from the top due to the rain yields not only a decrease in longwave cooling, but also in latent heat release and less cloud-top evaporation overall. Both categories consistently display a minimum buoyancy of around $0.5\,\mathrm{cm^2\,s^{-3}}$ in the sub-cloud layer, which is characteristic of the decoupling process, that occurs during the course of the SCT. Note that while no full buoyancy flux reversal is visible, this

https://doi.org/10.5194/egusphere-2026-479
Preprint. Discussion started: 29 January 2026

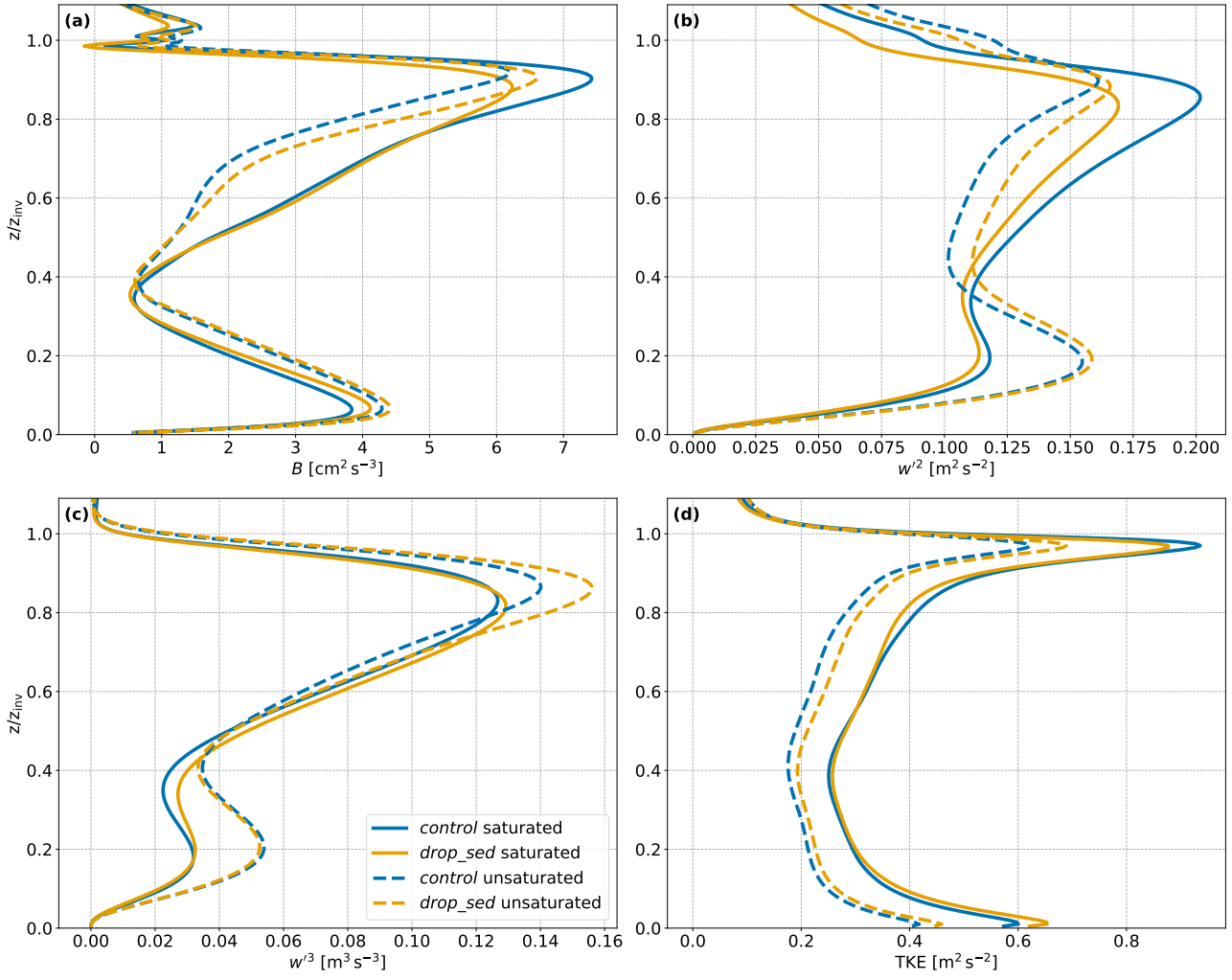

Figure 5. Total mean relative profiles of the **(a)** buoyancy flux B, **(b)** vertical wind variance w'^2, **(c)** third moment of the vertical wind w'^3 and **(d)** turbulent kinetic energy (TKE). Lines and colours as in Fig. 4.

is a mean profile of eight cases over a period of $42\,\mathrm{h}$. Full individual decoupling represented by negative buoyancy fluxes does in fact occur in the later stages of the simulation of each leg.

The corresponding minimum is also apparent in the vertical wind variance w'^2 in panel (b), although less distinctive in the saturated category. The same overall observations can be made here. While the unsaturated legs show an increase in w'^2 across nearly the entire boundary layer, the saturated legs display a consistent decline in w'^2, indicating that turbulence is increased in the former and reduced in the latter. Comparing the profiles of w'^2 and q_c in Fig. 4, they follow the same trend. In the unsaturated cases, both quantities increase, while in the saturated cases, both quantities decrease in the stratiform cloud layer. This correlation between q_c and w'^2 in the presence of cloud water sedimentation was also found in other studies. Bretherton

https://doi.org/10.5194/egusphere-2026-479
Preprint. Discussion started: 29 January 2026

et al. (2007); Pistor and Mellado (2025) simulated a non-precipitating, low-LWP case and observed an enhancement of both q_c as well as w'^2, aligning with the results of our unsaturated cases. On the other hand, Ackerman et al. (2009) found a q_c profile similar to that of our saturated cases, along with a reduction in w'^2 in their drizzling, high-LWP simulation. This resulted in an overall increased LWP, in contrast to the LWP reduction in our saturated cases. However, this apparent contradiction can be resolved by the respective amounts of precipitation. In the case of Ackerman et al. (2009), surface precipitation was around $0.2\,\mathrm{mm\,d^{-1}}$, while almost all of our saturated legs reach precipitation rates of $\gtrsim 1\,\mathrm{mm\,d^{-1}}$, consistent with the magnitude of Stevens et al. (1998); Savic-Jovcic and Stevens (2008). This much stronger precipitation quickly overwhelms the initial LWP increase, resulting in both reduced LWP and w'^2.

In panel (c), the third moment of the vertical velocity w'^3 is depicted. While the second moment of the vertical wind characterises the strength of turbulent fluctuations, the third moment describes the asymmetry between upward and downward motions. Positive (negative) w'^3 indicates strong and narrow updrafts (downdrafts), in the presence of generally weak and broad downdrafts (updrafts). For both categories, w'^3 is consistently positive throughout the boundary layer, implying that there is an overall weak subsidence disrupted by narrow updrafts. In the unsaturated cases, it increases in the presence of cloud droplet sedimentation across the cloud layer, pointing at even stronger, more concentrated updrafts. Together with w'^2, we can confidently say that in *drop_sed*, stronger updrafts drive vertical motions in the cloud. In contrast, w'^3 is only slightly enhanced in the saturated cases, and even unaffected in the upper levels of the cloud.

The full resolved TKE profile is presented in panel (d). The sub-grid scale contribution is small and exhibits the same behaviour, which is why it is omitted here. All profiles show the characteristic peaks near the inversion and at the surface, where the impact of shear is the strongest. Overall, it reinforces all our observations regarding *control* and *drop_sed* from before. In the unsaturated cases, the TKE is considerably increased in the entire boundary layer. In contrast, it is decreased in the cloud layer in the saturated cases and slightly enhanced towards the surface.

Based on these previous findings, we can construct the following process chain to explain the differences in entrainment outcomes among the two categories in the presence of sedimentation. In the initial stages, cloud droplet sedimentation leads to the expected and often observed result in all cases: entrainment is lowered, as droplets are removed from the inversion layer, reducing the potential for evaporative cooling. Accordingly, this is accompanied by an increase in LWP. After this initial period of a few hours, the individual cases split.

In the heavily precipitating saturated cases, the trend of reduced boundary layer growth continues, as droplet sedimentation enhances rain formation. Rain acts to lower convective intensity, as latent heat release near the top and latent heat consumption below cloud-base impede turbulent circulations. Furthermore, it drains the cloud of liquid water, which overwhelms the initial increase in the present cases. Thus, the initial weaker boundary layer growth is amplified and continues until the end of the simulation (or the breakup of the cloud deck).

In the unsaturated cases without strong precipitation, neither the TKE reduction nor the liquid water depletion occurs. Rather, the initial LWP increase induces additional longwave cooling, which is not yet saturated due to the small overall LWP. This leads to more potent turbulent circulations in the boundary layer, especially stronger and narrower updrafts, that can redis-

https://doi.org/10.5194/egusphere-2026-479
Preprint. Discussion started: 29 January 2026

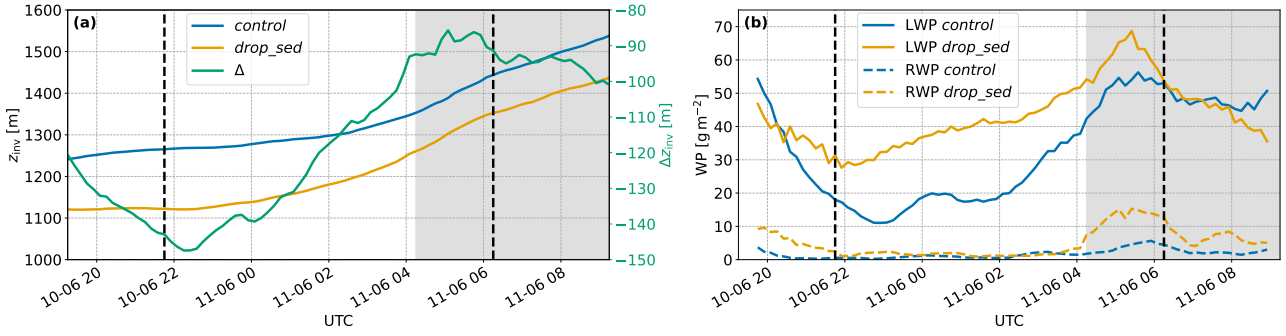

Figure 6. Time evolution of the **(a)** inversion height z_{inv} and **(b)** water paths (WP) of Leg 12A. The vertical dashed lines enclose the analysis period for this section. In panel (b), the solid lines depict the liquid water path (LWP), while the dashed ones depict the rain water path (RWP). For the water paths, a 1 h rolling mean was applied. Colours as in Fig. 3 and grey shading marks local night-time.

tribute moisture from the ocean surface and thereby enable more liquid water production. This turns into a feedback loop of more liquid water leading to more cooling leading to more turbulence leading to more liquid water, that counteracts the weak stabilising effect of rain. Since the sedimentation velocities in the unsaturated legs are low due to their small effective radii, the additional turbulence is able to transport liquid water all the way to cloud-top. This re-enables stronger evaporative cooling, which adds to the longwave cooling. As long as rain formation remains limited and the LWP is small enough for the radiative cooling to be unsaturated, this turbulence intensification prevails. Altogether, the enhanced convective intensity, supported by the evaporative cooling, promotes stronger entrainment and allows it to persist over an extended period of time.

4 Sensitivity tests

In our proposed mechanism, we identified drizzle formation as well as the amount of liquid water with regard to longwave cooling as the two crucial drivers. We now want to test the robustness and importance of these factors during individual periods as well as additional sensitivity experiments.

4.1 Leg 12A, unsaturated period

The previous investigations involving the averaged profiles evidently resemble overall behaviour, however, certain periods of individual deviations can be shadowed. Since we simulate two full days, the effect of the diurnal cycle is included in our runs. Especially the day-time thinning of the cloud deck in the saturated legs can have a profound impact on the LWP, and also potentially shift the leg from the saturated to the unsaturated category. One example, which is even visible in panel (a) of Fig. 3, is the period between 2200 km and 2400 km. Here, the continuous decline of Δz_{inv} is interrupted by a period of strong increase, indicating enhanced entrainment. As evident from Table 1, only Leg 12A contributes this far off the coast, implying this is an individual feature of this leg, that we can analyse.

https://doi.org/10.5194/egusphere-2026-479
Preprint. Discussion started: 29 January 2026

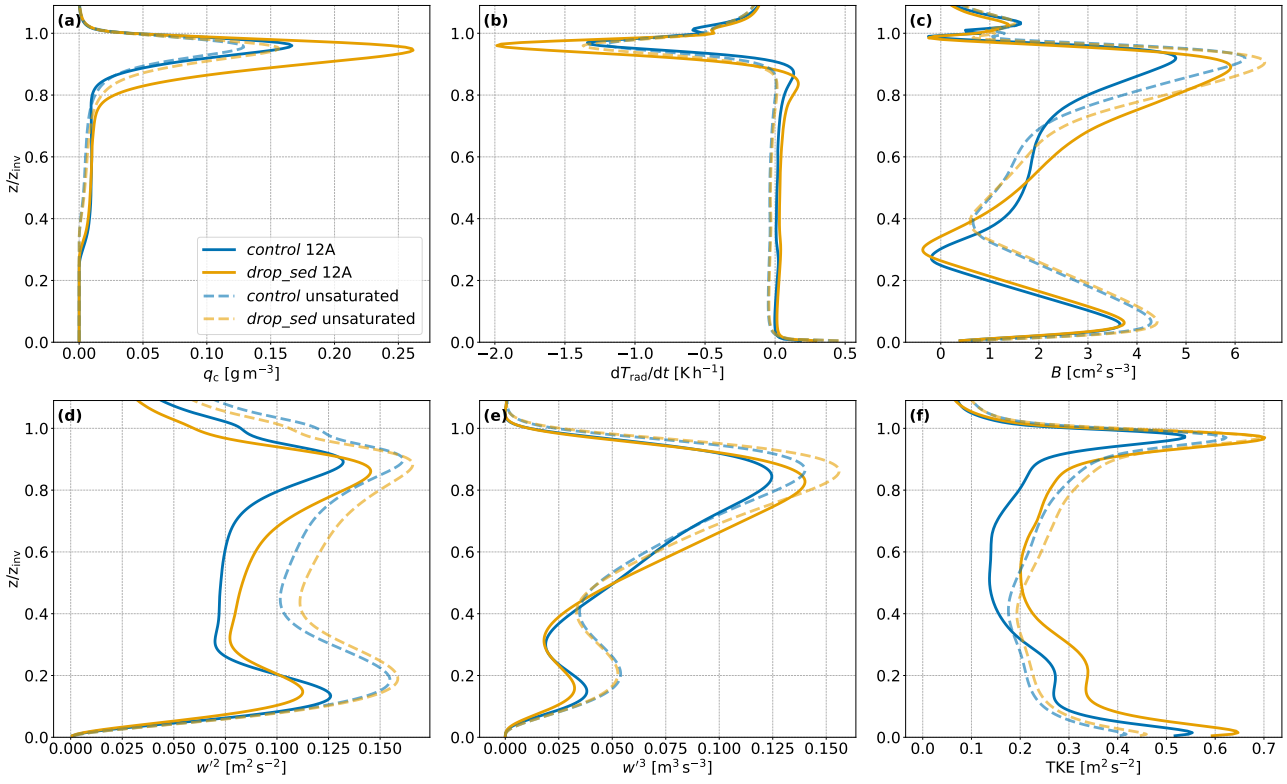

Figure 7. Total mean relative profiles of the **(a)** liquid water content q_c, **(b)** radiative heating rate $\mathrm{d}T_{\mathrm{rad}}/\mathrm{d}t$, **(c)** buoyancy flux B, **(d)** vertical wind variance w'^2, **(e)** third moment of the vertical wind w'^3 and **(f)** turbulent kinetic energy (TKE). The solid lines represent Leg 12A in the unsaturated period, while the transparent dashed lines represent the full unsaturated profiles for comparison. Colours as in Fig. 4.

For clarification, we displayed z_{inv} of Leg 12A in this time period in panel (a) of Fig. 6. The vertical dashed lines mark the interval of increased entrainment in the *drop_sed* run, that we analyse in the following. We decided to extend this interval a little further than the extremes to also capture the initial and final stages more accurately. The steady increase between the two extremes of Δz_{inv} corresponds to a mean acceleration of w_{e} of 18% over the course of $7\,\mathrm{h}$. This acceleration is not only substantially larger than the previous amplification of around 10% in the case of Leg 04A, but also in the vicinity of the strongest individual reduction of an individual leg of around 20%. In panel (b), both LWP and RWP in this period are depicted. The overall amount of LWP is well within the range, where longwave cooling is not saturated, until the beginning of the second night. The low values are the result of the day-time thinning through solar insolation, combined with strong precipitation. The latter declines simultaneously and arrives at almost no rain at the start of the chosen interval. While the LWP was larger in the *control* run before, this flips and reaches values more than twice as high in the *drop_sed* run. At the end of the day, the overall magnitude of the LWP increases again, supporting the rain formation in *drop_sed*. As soon as the RWP is substantially increased in *drop_sed*, the corresponding LWP declines and becomes once again lower than in *control*, marking the end of the interval.

https://doi.org/10.5194/egusphere-2026-479
Preprint. Discussion started: 29 January 2026

Following the analysis in Sect. 3.3, Fig. 7 shows the different relative profiles. The solid lines represent the relative profiles for Leg 12A in the selected period marked by the dashed vertical lines in Fig. 6. Furthermore, we added the full unsaturated profiles from Figs. 4 and 5 in fainter dashed lines as a reference. Without repeating the details regarding individual profiles, it is evident that all six Leg 12A profiles behave analogously to the unsaturated cases. During this period, q_c, longwave cooling as well as the turbulence quantities are considerably increased. Especially the former two show an even stronger amplification for Leg 12A than for the unsaturated legs, which is possible thanks to the absence of rain. This leads to a pronounced increase in TKE throughout the entire boundary layer, promoting entrainment in the *drop_sed* run. These results firmly support the proposed feedback loop from Sect. 3.3, confirming that enhanced longwave cooling is a main driver in regions of low LWP.

4.2 Non-precipitating cases

In order to further evaluate the proposed mechanism, we conduct three more sensitivity experiments, the first one targeting precipitation. Precipitation in stratocumuli has a profound impact on boundary layer dynamics. Stevens et al. (1998) showed that heavy drizzle substantially reduces entrainment through a reduction in turbulent kinetic energy. As drizzle forms, latent heat is released in the cloud through condensation, warming the cloud layer. When the rain drops sediment out of the cloud, evaporation leads to cooling in the sub-cloud layer. This combination restrains deep circulations and supports the formation of cumuli below the original stratocumulus deck. These results were largely confirmed in the large-domain LES study by Savic-Jovcic and Stevens (2008), where also a reduction in TKE as well as boundary layer growth was observed in the presence of strong drizzle.

In our simulations, all saturated cases are strongly drizzling for a certain period of time, whereas only very limited drizzle forms in the unsaturated ones. This can be directly attributed to the differences in the amount of liquid water in the clouds. The surface precipitation rates for the representative legs can be found in panels (a) and (b) of Fig. 8, respectively. Leg 16A features substantial drizzle rates from the beginning, with a considerable drop during the first day due to the day-time thinning of the cloud deck. Moreover, in the *drop_sed* runs, precipitation formation is generally enhanced because of the sedimenting droplets, which was also observed by Ackerman et al. (2009). In contrast, Leg 11A only develops a sizeable amount at the end of the second night, which is again substantially larger in the *drop_sed* run. This strong increase is also responsible for the abrupt drop in the *drop_sed* inversion shown in panel (d), since the rain drops not only reduce the available TKE, but also simply deplete the cloud of liquid water (Stevens et al., 1998; Savic-Jovcic and Stevens, 2008; Ackerman et al., 2009).

To rule out the possibility that the absence of drizzle alone is responsible for the observed behaviour in the unsaturated cases, we performed two non-precipitating sensitivity runs for the representative legs. The resulting z_{inv} together with the precipitating runs can be found in the bottom panels (c) and (d) of Fig. 8. Comparing the impact during Leg 16A, there is a clear difference after the first night. While the precipitating case shows only a weakened divergence in Δz_{inv} during the first day, the non-precipitating case actually shows a weak, but continuous, enhanced boundary layer growth in the *drop_sed* case. After this period of faster growth, it roughly stabilises until the end, leading to an overall lower boundary layer in the non-precipitating *drop_sed* run. So after the strong initial decrease in entrainment, Δz_{inv} in the non-precipitating runs remains similar, with periods of slightly increased or reduced boundary layer growth. This reflects the counteracting effect of the sedimenting droplets

https://doi.org/10.5194/egusphere-2026-479
Preprint. Discussion started: 29 January 2026

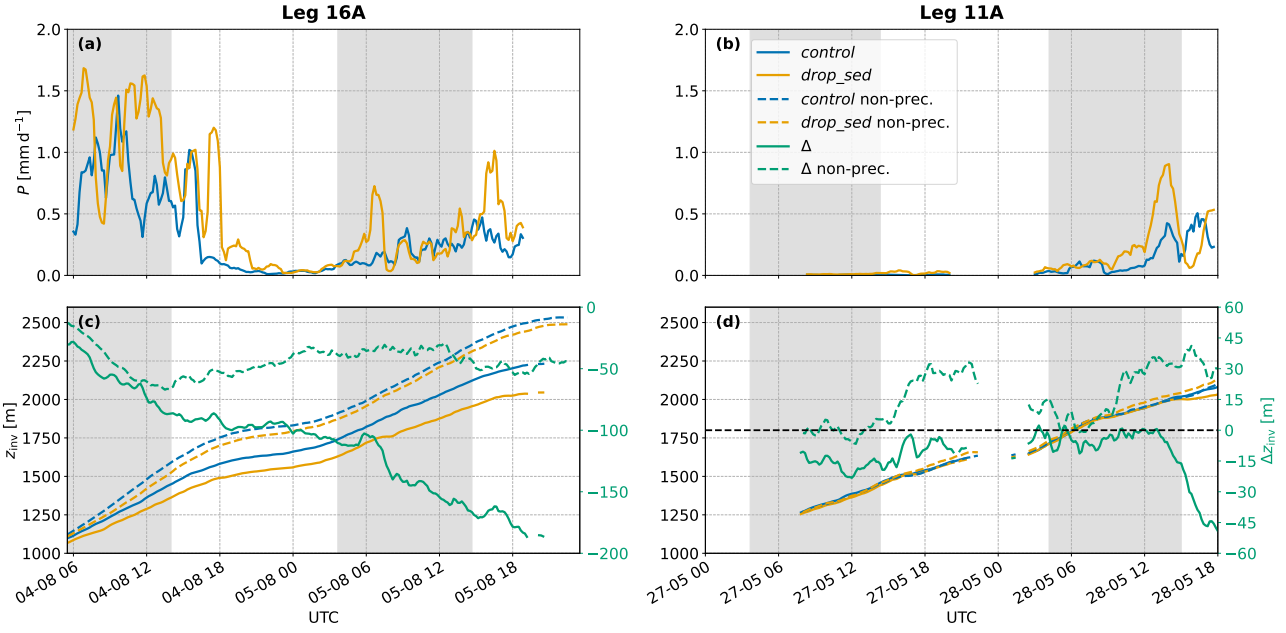

Figure 8. Comparison of the representative legs for the saturated category (Leg 16A, left) and unsaturated category (Leg 11A, right). The top panels **(a)** and **(b)** show the precipitation rates P, while the bottom panels **(c)** and **(d)** show the results for the inversion height z_{inv}, respectively. For the precipitation rates, a 1 h rolling mean was applied. The solid lines represent the precipitating runs, whereas the dashed lines represent the non-precipitating runs. Colours are the same as in Fig. 3 and the grey shading marks local night-time.

and the enhanced turbulence, where the latter is now not affected by precipitation. During the stronger entrainment phase, there is a lot more liquid water near cloud-top (cf. Fig. 10, panel (b), green line) leading to enhanced evaporative cooling and thus, stronger turbulence in the entrainment zone. Furthermore, during the day, the LWP drops substantially into the regime of unsaturated longwave cooling, while still being considerably enhanced in *drop_sed* (cf. Fig. A4). This way, the overall cooling is not only redistributed, but also magnified and the amplified turbulence can work against the sedimenting droplets. After that period, the sedimentation balances out the increased turbulence, as the cloud enters the saturated regime during the second night again and cloud water is not longer enhanced in the cloud-top region. This situation can be seen as an unstable equilibrium of the sedimenting droplets reducing entrainment and the enhanced LWP counteracting it by amplifying turbulent circulations.

For Leg 11A, the situation is different. Both runs commence around the same z_{inv}, followed by two episodes of strongly increasing Δz_{inv}, with an intermission of decreasing Δz_{inv}. So even though almost no drizzle drops are present in the beginning, the inclusion of rain processes alters the base state of the stratocumulus deck. Furthermore, the lack of rain enables even faster entrainment in the *drop_sed* case until the middle of the first day, after which solar insolation dries out the deck. The fact that the *control* inversion grows faster in this period might by a consequence of the almost vanishing cloud. After the reformation is complete, *drop_sed* entrains faster again, resulting in a net raised cloud-top height after the full 48 h.

https://doi.org/10.5194/egusphere-2026-479
Preprint. Discussion started: 29 January 2026

In summary, the overall impact of precipitation can mask and overwhelm the enhanced entrainment effect of sedimentation in the unsaturated cases, if substantial amounts of drizzle form. However, we can infer from the analysis of Leg 16A, that even though drizzle plays a large role in reducing entrainment, it is not solely responsible for reduced entrainment in simulations with activated cloud droplet sedimentation. Rather, sedimentation reinforces drizzle that decreases entrainment, while the non-precipitating saturated case shows that the additional liquid water can balance out the original sedimentation-entrainment feedback after the initial period. In contrast to the consistent entrainment increase in Leg 04A, this outcome is unstable, since it lacks the amplification of longwave cooling as an additional driver of turbulence.

4.3 Unsaturated case with low background CCN

The second sensitivity experiment examines the influence of the cloud condensation nuclei (CCN) background in the individual transects. CNN are among the important factors regulating precipitation onset, as the amount of cloud droplets is directly dependent on the number of CCN. In general, higher CCN concentrations yield more and smaller cloud droplets and thus, thicker clouds (e.g., Twomey, 1977; Twomey et al., 1984; Albrecht, 1989). In the Northeast Pacific, the CCN concentration declines towards the open ocean, as the influence of continental pollution diminishes. This westward decrease has also been observed during the MAGIC campaign (Painemal et al., 2015; Brendecke et al., 2022). As mentioned in Sect. 2.1, we used a background CCN concentration of $250\,\mathrm{cm}^{-3}$ for all legs, which is a solid approximation for the saturated legs in our $48\,\mathrm{h}$ window (Painemal et al., 2015). Apart from Leg 12A, these simulations either terminate or the stratocumulus deck breaks up no later than $138.2\,^{\circ}\,\mathrm{W}$ (cf. Table 1). However, for parts of Leg 04A and especially for Leg 11A, this value exceeds the acceptable range. The latter leg starts outside the continental influence and is further a low CCN leg (Painemal et al., 2015). To address this issue, we repeated the Leg 11A runs with the ICON maritime setting of a background CCN concentration of $100\,\mathrm{cm}^{-3}$. We did this both in the precipitating and the non-precipitating setup to observe possible changes in both cases. Before discussing the results, it is worth noting that CCN concentrations are not the primary driver behind the observed saturated and unsaturated categories. The likely more important drivers are large-scale synoptic conditions impacting temperature and humidity. Most of the saturated legs form under a strong inversion with cold and moist inflow from the North. In contrast, this inflow is considerably attenuated in the unsaturated legs, yielding thinner cloud decks with weaker inversions.

The resulting z_{inv} can be found in Fig. 9. The precipitating case shown in panel (a) exhibits a similar evolution in the low CCN scenario with a weaker growing z_{inv} in the *drop_sed* case. However, on closer inspection, the period of continuously stronger entrainment during the first day in the *drop_sed* case of the standard CCN scenario is not distinctly present in the low CCN one. Rather, an overall weaker growing boundary layer with brief intermittent bursts of stronger entrainment is observed, resulting in a decreasing trend of Δz_{inv}. It can also be seen from the disappearance of the dashed line in the second night, that the cloud fraction of the stratocumulus deck drops below $40\,\%$ and does not recover until the end. This development can be explained by the altered precipitation behaviour. The maximum *drop_sed* surface precipitation rate of below $1\,\mathrm{mm\,d}^{-1}$ is reached at the end of the second night in the standard CCN scenario (cf. Fig. 8, panel (b)). In the new experiment, this value is surpassed at the beginning of the second night and increases up to almost $1.5\,\mathrm{mm\,d}^{-1}$ in both *control* and *drop_sed* (not

https://doi.org/10.5194/egusphere-2026-479
Preprint. Discussion started: 29 January 2026

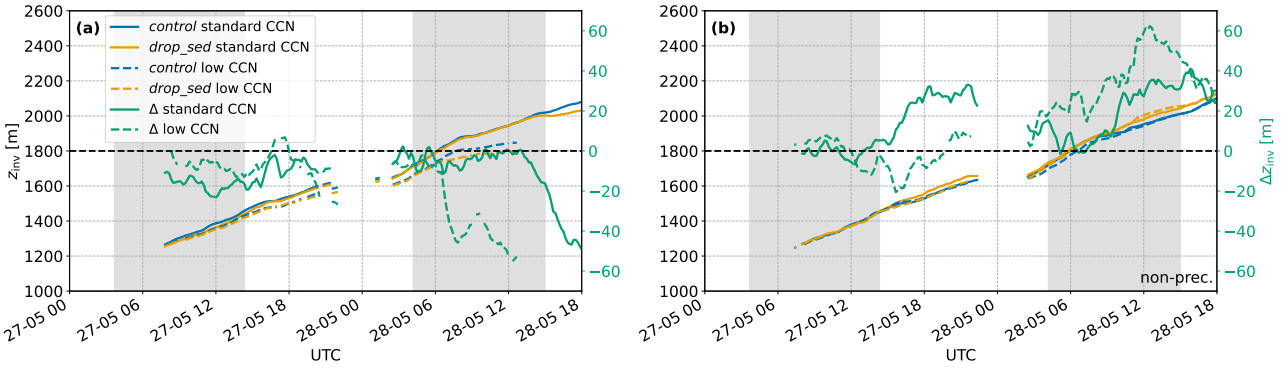

Figure 9. Inversion heights z_{inv} of the **(a)** precipitating and **(b)** non-precipitating low CCN sensitivity experiments for Leg 11A. Colours and shading as in Fig. 8. The solid lines represent the standard CCN scenario ($250\,\mathrm{cm}^{-3}$), while the dashed lines represent the low CCN scenario ($100\,\mathrm{cm}^{-3}$).

shown). The lower CCN concentrations facilitate rain formation due to the larger droplets, which is in accordance with earlier findings from e.g. Feingold et al. (1999). The resulting strengthened decoupling leads to the observed reduced boundary layer growth in the low CCN scenario. Additionally, the continuous negative divergence of Δz_{inv} can be explained by the overall enhanced rain formation in the *drop_sed* case. As for the saturated legs, the reinforcement of rain in combination with the sedimenting droplets is stronger than the amplified turbulence and we observe overall less entrainment. It should be noted that this effect is less pronounced than during the saturated legs, because drizzle formation is still suppressed in the beginning due to the low overall LWP. Thus, the latter is still periodically enhanced in *drop_sed* and the resulting stronger circulations can (partially) balance out the slow sedimentation velocity combined with the weak drizzle.

In the non-precipitating scenario of the different CCN cases in panel (b), the dashed blue and orange lines remain close to the solid ones, in contrast to panel (a). This is because rain is absent and cannot interfere with the cloud dynamics, which leads to a very similar development of the dashed and the solid curves. Comparing Δz_{inv}, the evolution of the dashed and the solid line is slightly different. Instead of the exchanging periods of increased and decreased entrainment, there is an initial decline in entrainment in the *drop_sed* run, followed by a continuous amplification and a final decline. While less CCN clearly influence the quantitative cloud development, the overall stronger entrainment in the *drop_sed* run, even leading to a deeper boundary layer, remains unchanged.

In general, we can conclude that the low CCN scenario does not yield structurally different outcomes. It slightly modified the course in the non-precipitating setup and reinforced drizzle formation in the precipitating one. This does produce a considerably different outcome in the latter, but this is not in conflict with our proposed process chain. It rather shifts this leg into the regime, where precipitation-induced stabilisation additionally works against the enhanced turbulence feedback loop and takes over earlier.

https://doi.org/10.5194/egusphere-2026-479
Preprint. Discussion started: 29 January 2026

Table 3. Mean cloud droplet sedimentation velocities $v_{\mathrm{sed},75}$ in the $75\,\mathrm{m}$ below the inversion over the whole course of the individual transects. The subscript v_{sed} refers to the sensitivity experiment where the sedimentation velocity was halved.

	default			non-precipitating		
case	11A	16A	16A$_{v_{\mathrm{sed}}}$	11A	16A	16A$_{v_{\mathrm{sed}}}$
$v_{\mathrm{sed},75}$ [$\mathrm{cm\,s^{-1}}$]	0.71	1.02	0.52	0.74	1.48	0.71

4.4 Saturated case with reduced sedimentation velocity

The last sensitivity experiment targets the magnitude of the sedimentation velocity. As sedimentation reduces entrainment, higher sedimentation velocities should evidently lead to a stronger reduction (Bretherton et al., 2007; Ackerman et al., 2009; Pistor and Mellado, 2025). Table 3 summarises the mean cloud droplet sedimentation velocities in the top $75\,\mathrm{m}$ of the representative legs. For Leg 11A, $v_{\mathrm{sed},75}$ is about two thirds of Leg 16A in the precipitating case, and half of it in the non-precipitating case. As the cloud in the non-precipitating Leg 16A run contains much more liquid water (cf. Fig. A4), the effective radii are larger and the sedimentation velocities are higher compared to the precipitating case. In contrast, Leg 11A lacks this feature, as there is almost no precipitation anyway. In general, the unsaturated cases have substantially smaller sedimentation velocities due to their lower effective radii.

To emulate the impact of the sedimentation strength of an unsaturated leg on a saturated leg, we conducted two sensitivity runs (precipitating and non-precipitating) for Leg 16A. In these simulations, we artificially halved the sedimentation velocity in the ICON microphysics. The resulting mean sedimentation velocity can be found in the respective third columns of Table 3. Clearly, the manual scaling by a factor of 0.5 does not yield a precise halving of the individual sedimentation velocities, as this introduces additional feedbacks. However, on average, the overall mean reduction is around $50\,\%$, which is similar or even smaller than $v_{\mathrm{sed},75}$ of Leg 11A.

Panel (a) of Fig. 10 shows the corresponding Δz_{inv}, that are each calculated with the respective *control* run (i.e. either precipitating or non-precipitating). Comparing the precipitating cases, the reduced sedimentation difference (orange) follows the same course as the original one (blue). On closer inspection, it is noticeable that this remarkably occurs at almost exactly half the value for the entire transect. Similarly, the precipitation rate differences (dashed) are also roughly halved, confirming the direct impact of v_{sed} on drizzle production (Ackerman et al., 2009). This further implies that, even in the case of lower sedimentation speeds, drizzle dominates boundary layer deepening in the saturated cases and yields a constantly slower boundary layer growth rate. However, the amount of drizzle production seems to be directly determined by the sedimentation velocity. The drizzle dominance is also visible, when comparing the precipitation curves to $\Delta q_{\mathrm{c},75}$ in panel (b). All four main periods, where blue is clearly above orange in the former, largely coincide with an inverse behaviour of the latter. This is the direct effect of strong drizzle depleting cloud-top of liquid water.

For both non-precipitating cases (green, magenta), the only consistent decrease of Δz_{inv} occurs during the initial period until

https://doi.org/10.5194/egusphere-2026-479
Preprint. Discussion started: 29 January 2026

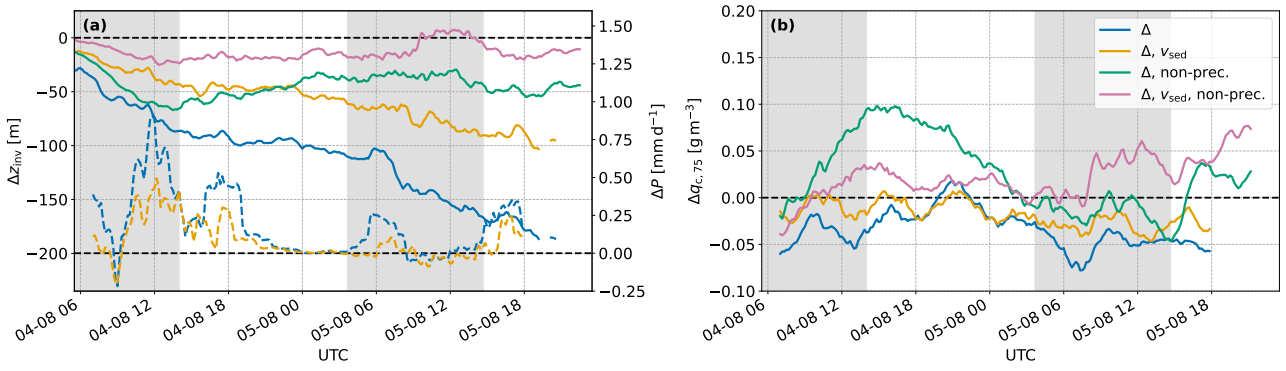

Figure 10. Leg 16A difference plots for **(a)** the inversion height z_{inv} (solid) as well as the precipitation rate P (dashed) and **(b)** the mean liquid water content in the top 75 m of the cloud $q_{\mathrm{c},75}$. The blue line and the green line are the respective differences in the default precipitating and the default non-precipitating setup (cf. Fig. 8, panel (c) for z_{inv}). The orange line and the magenta line are the analogous respective differences, but with a halved sedimentation velocity in the *drop_sed* run. All lines apart from z_{inv} were smoothed by a 3 h rolling mean. Shading as in Fig. 8.

the end of the first night. Analogously to the precipitating cases, this is weakened in the halved v_{sed} case (magenta), which roughly stabilises afterwards, implying that both runs entrain similarly. At the end of the second night, the stable period is interrupted by a period of increased entrainment in the *drop_sed* run, that even briefly yields a higher net cloud-top height. Taking into account panel (b), the latter can be explained by a sudden excess in $\Delta q_{\mathrm{c},75}$ during the second night, enabling stronger entrainment in the *drop_sed* run through evaporation. Furthermore, we can disentangle the other individual differences in the non-precipitating simulations. Interestingly, until the end of the first day, the simulation with the halved sedimentation speed ends up at lower amounts of liquid water near cloud-top (magenta below green) and also less LWP overall (cf. Fig. A4, dashed green vs. dashed orange). We can infer from this that the second-order liquid water reinforcement effect of the sedimenting droplets seems to be more powerful than the net loss of liquid water near cloud-top directly through sedimentation. In other words, even if v_{sed} is higher and should deplete cloud-top more efficiently, the increased q_{c} through the turbulent moisture redistribution can overcome this in the present saturated case and yield a higher amount of liquid water near the top, strengthening the potential for evaporative cooling. These differences between green and magenta in panel (b) account for the steady rise of the green curve and the relatively stable magenta curve in panel (a).

We can conclude that the initial decrease in Δz_{inv} is evidently driven by v_{sed}. After the initial stages, its major impact on precipitation continues, which drives the evolution in the drizzling simulations. In contrast, in the non-precipitating runs, it seems that after the initial period an unstable equilibrium is reached. This equilibrium appears to be largely unaffected by the magnitude of the sedimentation velocity in a direct way. It is, however, dependent on the base states of cloud liquid water near the top, which critically depend on the initial sedimentation speeds.

https://doi.org/10.5194/egusphere-2026-479
Preprint. Discussion started: 29 January 2026

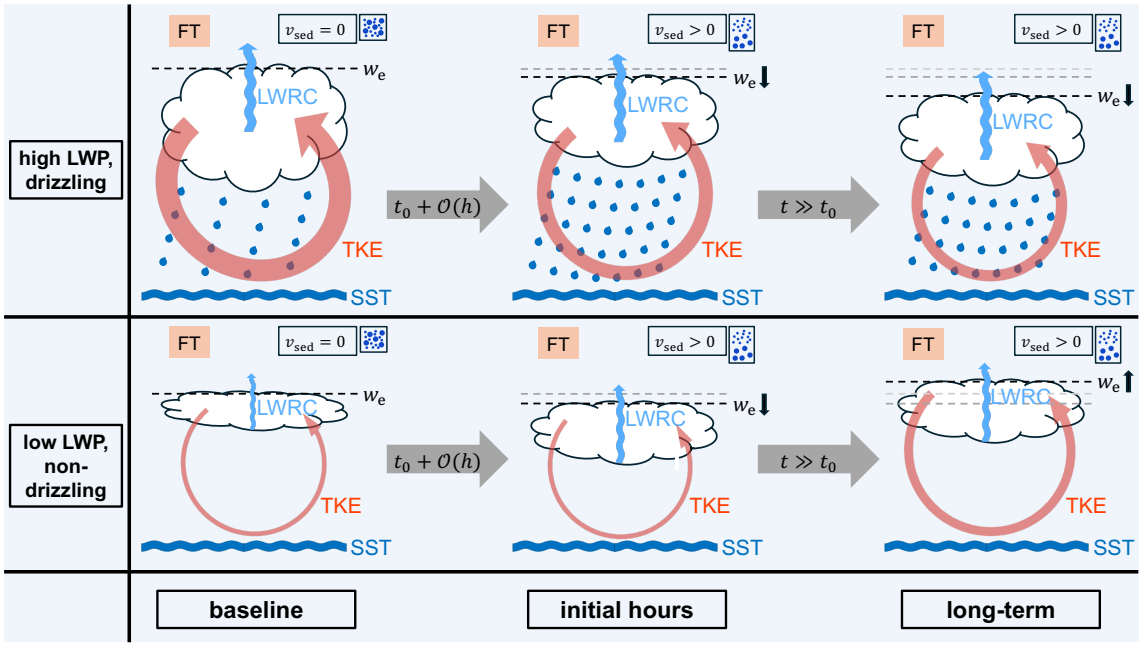

Figure 11. Schematic to illustrate to impact of droplet sedimentation on the two different idealised cloud categories (**top:** saturated and precipitating, **bottom:** unsaturated and non-precipitating). Both show a similar initial effect regarding entrainment, but evolve structurally different afterwards. The first stage is the baseline state at time t_0 before sedimentation is activated (indicated by v_{sed}), which also serves as the reference development in the *control* case. The middle stage is the state in the initial hours and the last stage is the state after a longer period of time. The cloud thickness is a rough measure of the liquid water path (LWP), the light blue arrows indicate longwave radiative cooling (LWRC), while the red arrows indicate turbulent circulations (turbulent kinetic energy, TKE). The ocean surface is illustrated by blue waves (sea surface temperature, SST). Dashed lines represent the inversion height z_{inv} under the dry free troposphere (FT), where entrainment occurs (marked by w_{e}), with states from previous time steps in grey (the fainter, the older), while the arrow thickness represents the strength of the respective quantity. Note that the light blue arrows are intentionally placed in the middle (bottom) of the cloud, if radiative cooling is saturated (unsaturated).

5 Discussion

In this study, we investigated the effect of cloud droplet sedimentation on the initial deepening stage of the stratocumulus to cumulus transition in 10 cases of the MAGIC campaign. While we could confirm the previously known entrainment reduction (Bretherton et al., 2007; Wyant et al., 2007; Ackerman et al., 2009; Hill et al., 2009; de Lozar and Mellado, 2017; Pistor and Mellado, 2025) in the initial hours for all simulated legs, we found a different development on longer timescales. After the initial stage, the cases split into groups of precipitating, high-LWP legs (saturated) versus non-precipitating, low-LWP legs (unsaturated). The general evolution for either category in the *drop_sed* cases is illustrated in Fig. 11, where the later stages should be interpreted relative to the *control* case in the base state. It is assumed for simplicity that the saturated (unsaturated) legs always (never) precipitate.

https://doi.org/10.5194/egusphere-2026-479
Preprint. Discussion started: 29 January 2026

The top panels summarise the evolution of the saturated legs. In the initial stages after the activation of sedimentation, the cloud droplets sediment away from cloud-top, leading to reduced evaporative cooling and thus, reduced entrainment. Furthermore, this enhances drizzle formation, which is why the expected increase in LWP is turned into a net decrease. The drizzle production impedes turbulent circulations, which further works against boundary layer growth. In the intermediate to long-term stages, this behaviour continues. The amplified drizzle reduces LWP as well as turbulence and together with the sedimentation-evaporation feedback, the entrainment rate is lowered. The total longwave cooling is roughly unaffected, as the cloud is saturated in every stage. The course of the unsaturated legs in the bottom panels starts in a similar way. The sedimenting droplets naturally reduce entrainment, which in this case yields an increase in LWP, as no drizzle is present. This in turn increases the total longwave cooling rate, since it is not saturated in these legs. From here, the initial phase smoothly transitions to the long-term phase. The additional longwave cooling introduces stronger turbulent circulations that maintain and also amplify the moisture supply from the ocean surface. This enhances LWP production, which completes the feedback chain of LWP, longwave cooling and turbulence. The resulting amplification of TKE in the boundary layer counteracts the sedimentation flux from the top and is able to push liquid upwards, which increases the potential for evaporative cooling. Eventually, this yields increased entrainment and can even lead to a higher boundary layer compared to the *control* case. In our simulations, we observe that this cycle can persist for more than one day and is strongly dependent on the amount of liquid water in the cloud and the strength of drizzle production.

In Fig. 11, the separation from the initial phase to the long-term phase is denoted by a timescale $t \gg t_0$. It is tempting to quantify this timescale, which is terminated by the onset of the turbulence feedback mechanism. Deriving a universal value proves difficult, as we only have two unsaturated cases to work with, one of which only starts to form a cloud late in the simulation. Furthermore, it is clear that this timescale is highly sensitive to various factors. The deciding factor here is the thickness of the cloud at the time of the activation of sedimentation, as not only the sedimentation velocity directly depends on it through droplet size, but also the increase in LWP and longwave cooling indirectly through the feedback mechanism. As evident from Fig. 9, the CCN concentration does not seem to interact with the initial decrease window, but suppressing precipitation does in the standard CCN scenario. Large-scale environmental conditions as e.g. the strength of the inversion (Sandu and Stevens, 2011) are likely to have an impact as well. With that in mind, we can extract the observed timescale for both unsaturated legs. For Leg 11A, the initial decrease in z_{inv} in the *drop_sed* run starts after the initial cloud formation at around 27.05., 06:00 and ends at 27.05., 12:00, yielding a $6\,\mathrm{h}$ period (e.g. Fig. 8, panel (d)). Remarkably, this agrees pretty well with the spinup experiment of Leg 04A (cf. Fig. A2) starting at 21.10., 09:00 and roughly terminating between 21.10., 14:00 and 21.10., 15:00, yielding a $5\,\mathrm{h}$ to $6\,\mathrm{h}$ period.

We identify this as the main difference from the simulations of Bretherton et al. (2007); Pistor and Mellado (2025), both of which simulated active droplet sedimentation for $6\,\mathrm{h}$. Their case from the first research flight (RF01) of the Second Dynamics and Chemistry of Marine Stratocumulus (DYCOMS-II) field campaign (Stevens et al., 2005) also belongs to the unsaturated category with a LWP of around $40\,\mathrm{g\,m^{-2}}$. Thus, based on our results, we would expect an increase in entrainment in the presence of droplet sedimentation after the initial period. The observed reduction in both Bretherton et al. (2007); Pistor and

https://doi.org/10.5194/egusphere-2026-479
Preprint. Discussion started: 29 January 2026

Mellado (2025) is not in contrast to our findings, if we take into account the identified initial phase of roughly $6\,\mathrm{h}$, where entrainment is also reduced in our MAGIC simulations. So given that droplet sedimentation yields increased entrainment after a somewhat different timescale, it is likely not yet visible in the above relatively short simulations. This also serves as an explanation for the fact that Bretherton et al. (2007); de Lozar and Mellado (2017); Pistor and Mellado (2025) found a negligible influence of longwave cooling. The short simulations are not able to capture the period, where the initial dominant impact of sedimentation is replaced by the turbulence feedback chain, with longwave cooling as a main contributor. Apart from that, there is also the third moment of the vertical wind, that structurally differs to our cases. While the profile w'^3 in Pistor and Mellado (2025) turns negative below cloud-base, it is also mostly reduced in the presence of sedimentation. In the present cases the mean w'^3 profile is always positive and increased (cf. Figs. 5, 7), pointing to a different organisation of up- and downdrafts. In contrast, we would not expect the LES result of Ackerman et al. (2009) to flip from the observed reduced to strengthened entrainment, if one would extend the simulation time. These simulations are not only precipitating, but also based on a different research flight (RF02) of DYCOMS-II with a LWP of around $100\,\mathrm{g\,m^{-2}}$, which is well in the saturated regime of longwave cooling.

While cloud albedo susceptibility is not the primary focus of this study, we would like to point out that the opposing changes in LWP between the two regimes lead to a mean decrease of -11.1 % in the pseudo-albedo when the cloud is saturated in the longwave, and a respective increase of 14.8 % when the longwave flux at cloud-top is not yet saturated. Even though this is only an overall mean, it underlines again that the effects in the unsaturated cases are opposite, but of similar strength as in the saturated cases. Thus, the mechanism suggested by Bretherton et al. (2007) regarding droplet sedimentation impacts on the LWP adjustment is still found to hold in more common thick clouds on timescales exceeding $6\,\mathrm{h}$.

Extending the discussion of high vs low LWP, we can address the importance of the two categories in reality. In doing so, we analyse one year of post-processed GOES 15 retrievals (Minnis et al., 2002, 2008, 2011) during the MAGIC period in the Northeast Pacific between $[20°\,\mathrm{N}, 35°\,\mathrm{N}]$ and $[117°\,\mathrm{W}, 160°\,\mathrm{W}]$. We choose this region to include the full MAGIC transects between Los Angeles at $[118.2°\,\mathrm{W}, 34.1°\,\mathrm{N}]$ and Honolulu at $[157.9°\,\mathrm{W}, 21.3°\,\mathrm{N}]$. Half-hourly day-time LWP data from 18:00 to 00:00 UTC are filtered for stratiform low clouds using the ISCCP thresholds of optical depth > 3.6 and cloud-top pressure $> 680\,\mathrm{hPa}$ (Rossow and Schiffer, 1999). Separating them by the LWP threshold of $50\,\mathrm{g\,m^{-2}}$ as in Table 1, we obtain roughly 23 % in the unsaturated category and 77 % in the saturated category. This result is in good agreement with the corresponding LWP distribution for the Northeast Pacific, as well as with those observed in other subtropical stratocumulus decks (Murakami et al., 2021). This highlights the prevalence of the saturated category, which also aligns with the present observation of eight saturated and two unsaturated cases. Thus, the majority of studies focusing on droplet sedimentation effects not only neglect longer timescales, but also concentrate on low-LWP cases, which constitute the minority of subtropical stratiform clouds (Bretherton et al., 2007; de Lozar and Mellado, 2017; Schulz and Mellado, 2019; Igel, 2024; Pistor and Mellado, 2025).

Lastly, we can speculate about the impact of droplet sedimentation on the complete transition of stratocumulus to cumulus. The present $48\,\mathrm{h}$ runs are not enough to capture a full SCT. However, there are some saturated legs, where the stratocumulus

https://doi.org/10.5194/egusphere-2026-479
Preprint. Discussion started: 29 January 2026

deck partially breaks up, indicated by its cloud fraction dropping below the 40 % threshold, and does not recover (cf. Table 1). As can be seen from Fig. A1, only for 07A, 13A, 14A and 17A this breakup occurs considerably before the end of the simulation. While all *drop_sed* runs consistently break up later, pointing at the enhanced sustainability of the cloud at low LWP, the specific timing is only marginally affected. The average delay of $\approx 40\,\mathrm{km}$ is strongly driven by the unstable winter case 07A, that shifts roughly $100\,\mathrm{km}$, while the three summer legs vary below $25\,\mathrm{km}$. Regarding the full deepening period of roughly $2000\,\mathrm{km}$, we observe only little change. Extending this to a potential reformation of the stratocumulus deck during night-times, we can use Leg 17A as a proxy, where we also observe no considerable alterations in *drop_sed* compared to the *control* run (not shown). We cautiously interpret this as the aforementioned counteracting effects of enhanced precipitation and enhanced turbulence balancing each other, as soon as the cloud deck enters the low LWP regime. In fact, the amplified drizzle through sedimentation is not enough to lead to a runaway precipitation-driven SCT, as was observed by Yamaguchi et al. (2017). Thus, we conclude that the impact of cloud droplet sedimentation on the SCT in the saturated legs regarding the qualitative initial deepening period is insubstantial and likely remains so in the later stages. There might be more substantial changes in the unsaturated legs, as they are more strongly affected by the presented mechanism. However, this heavily depends on the onset of drizzle, as found for Leg 11A. So while these effects might be more potent, we still expect them to be minor overall, also due the powerful influence of the large-scale conditions or the diurnal cycle.

6 Conclusions

This study addressed the impact of cloud droplet sedimentation in stratocumuli regarding longer timescales in the context of the stratocumulus to cumulus transition. We performed $48\,\mathrm{h}$ long large-eddy simulations in ICON along 10 selected MAGIC transects in the Northeast Pacific, conducting one *control* run and one with active cloud droplet sedimentation parametrisation for each case. We found the well-known entrainment reduction due to reduced evaporation in the initial hours of all cases, after which they show contrasting behaviour depending on their drizzle amount and LWP. The boundary layer in cases with high LWP and substantial precipitation continues to grow slower, reinforced by the stabilising effect of precipitation, while it rises faster in cases with low LWP and no precipitation. In the latter, the initial increase in LWP serves as the initiator for a feedback mechanism consisting of longwave radiative cooling, turbulent mixing and LWP. As the low-LWP clouds are not yet saturated in the longwave, the increase in LWP leads to an increase in net longwave cooling, which amplifies turbulent circulations. Those sustain the moisture supply for the cloud and further push liquid back to the entrainment zone, counteracting the direct depletion through the sedimenting droplets. As our simulations include two full days, we could demonstrate that high-LWP cases can transition to the other regime due to day-time thinning and experience the same mechanism, pointing towards a more robust and fundamental mechanism.

Sensitivity experiments disabling precipitation revealed that this effect is not solely a result of amplified drizzle in the *drop_sed* case. The LWP increase in the high-LWP cases does not have a strong impact on the already saturated longwave cooling, so that the feedback chain is suppressed and both the *control* run and the *drop_sed* run entrain similarly. Furthermore, we could show that the magnitude of the sedimentation velocity only drives the initial entrainment reduction, but has little impact on

https://doi.org/10.5194/egusphere-2026-479
Preprint. Discussion started: 29 January 2026

the longer timescales. In a third sensitivity experiment, we found that the background CCN concentration does not change the qualitative process chain either.

There are two important implications of our findings. Firstly, it is difficult to generalise results from a limited amount of cases, when studying the impact of a specific process. Regarding droplet sedimentation in subtropical stratocumuli, the majority of studies simulate one case with low LWP, while neglecting that this regime only represents the minority in reality. We acknowledge that the present 10 cases are not a large sample either, however, we could include synoptic variability and provide some statistics, that revealed clear regime differences. In general, it is important to incorporate various cases in the analysis in order to capture different mechanisms. Secondly, the common approach of studying the impact of droplet sedimentation in simulations of only a few hours obscures the long-term effect, which we have shown can be profoundly different from the initial hours.

Code and data availability. The ICON model is open source and can be downloaded from https://www.icon-model.org/. The specific version used in this study together with the input can be obtained from the authors upon request. The initial conditions and the large-scale forcings are based on the original forcings by McGibbon and Bretherton (2017) (https://github.com/GdR-DEPHY/DEPHY-SCM/tree/master/MAGIC, accessed: Feb. 2024) and were adapted for ICON. The data from the MAGIC campaign are available at https://www.arm.gov/, while the post-processed GOES 15 data are available from armarchive@arm.gov upon request. The data to create the plots will be uploaded to Zenodo upon final publication.

https://doi.org/10.5194/egusphere-2026-479
Preprint. Discussion started: 29 January 2026

Appendix A: Additional figures

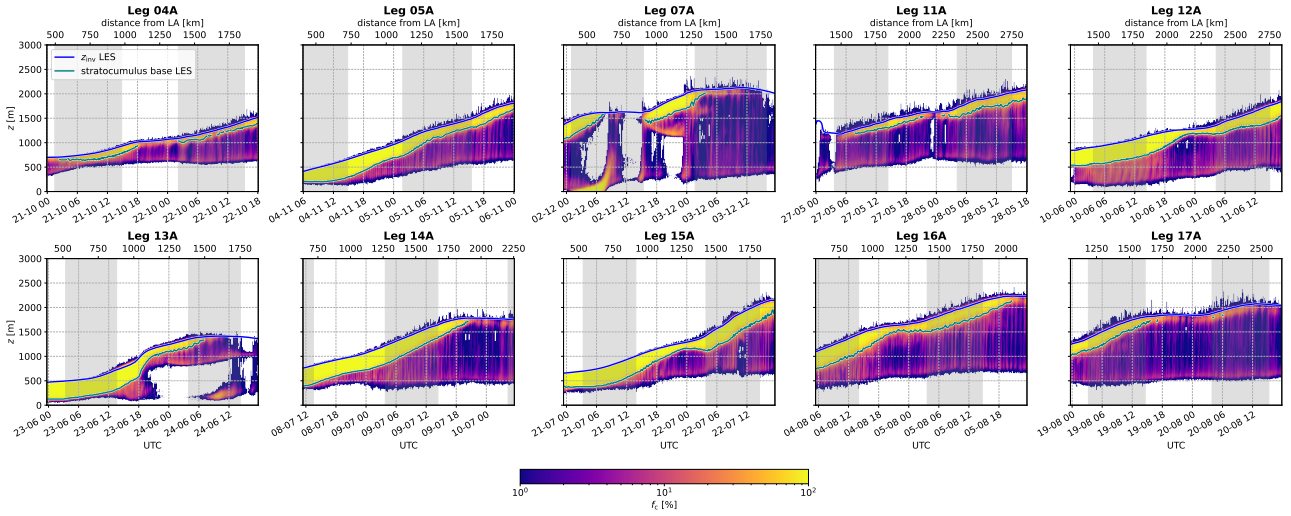

Figure A1. Domain-averaged cloud fraction f_c of the *control* runs for all legs. Colours and shading as in Fig. 1.

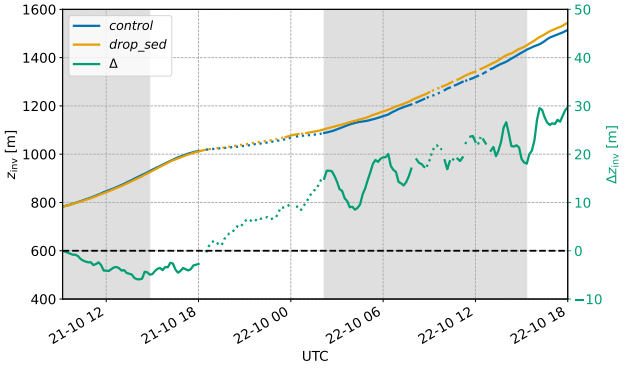

Figure A2. Leg 04A inversion height z_{inv} of the long spinup experiment. Colours and shading as in Fig. 3. The dotted periods correspond to the stages where the mean cloud fraction is below $40\,\%$.

https://doi.org/10.5194/egusphere-2026-479
Preprint. Discussion started: 29 January 2026

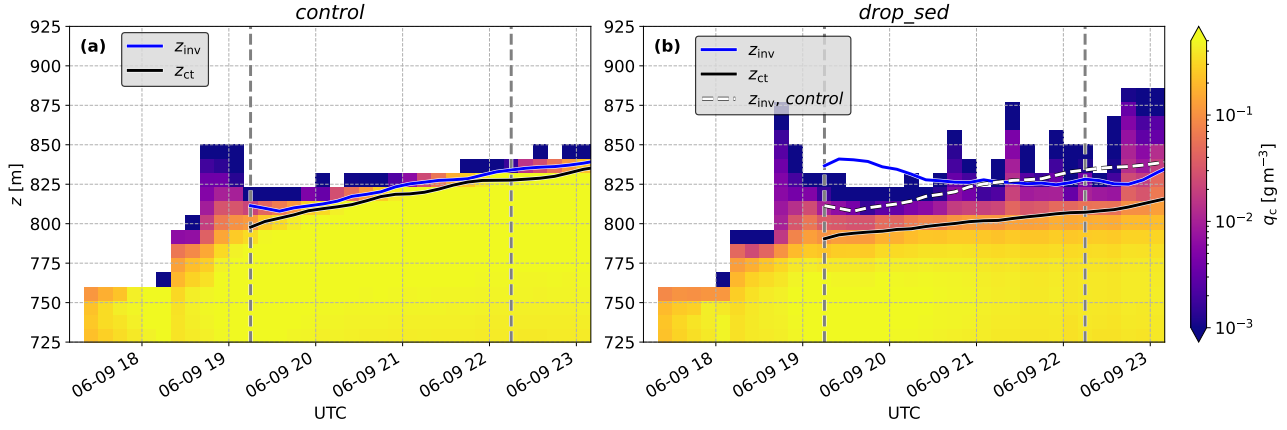

Figure A3. Leg 12A liquid water content q_c together with inversion height z_{inv} and cloud-top height z_{ct} for the **(a)** *control* and **(b)** *drop_sed* simulation. The grey dashed lines mark the period analysed in Table 2. For clarity, the *control* inversion is shown as a white dashed line in panel (b).

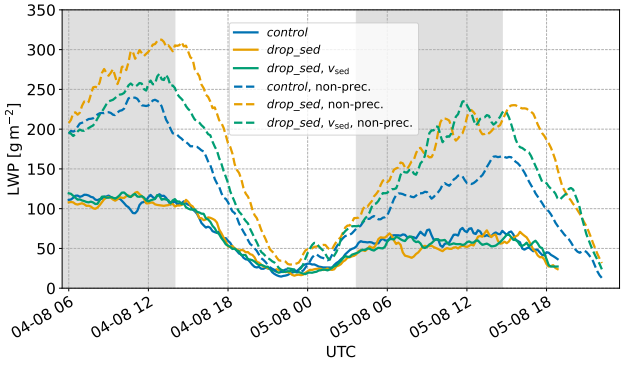

Figure A4. Leg 16A liquid water path (LWP) for the *control* (blue), *drop_sed* (orange) and halved sedimentation speed (green) experiments, including the precipitating (solid) and non-precipitating (dashed) simulations. A 1 h rolling mean was applied to all lines. Shading as in Fig. 3.

https://doi.org/10.5194/egusphere-2026-479
Preprint. Discussion started: 29 January 2026

Author contributions. MS conducted the simulations, analysed the data and wrote the initial draft. MA and MS designed the simulation setup. AP conceived the project and acquired the funding. All authors commented on the manuscript.

Competing interests. One author is member of the editorial board of ACP. Other than that, the authors declare no conflict of interest.

Acknowledgements. MS would like to thank Axel Seifert for his expertise regarding the implementation of droplet sedimentation in ICON and Peter Blossey for his valuable assistance with the creation of the large-scale forcings. MS and AP appreciate support from the Hans Ertel Centre for Weather Research (Hans-Ertel-Zentrum für Wetterforschung; HErZ) funded by the Federal Ministry of Transport (grant number: 4823DWDP7). MA acknowledges support from HErZ and the German Weather Service (Deutscher Wetterdienst, DWD). This work used resources of the German Climate Computing Centre (Deutsches Klimarechenzentrum, DKRZ) granted by its Scientific Steering Committee (WLA) under project ID 1358.

https://doi.org/10.5194/egusphere-2026-479
Preprint. Discussion started: 29 January 2026

References

Ackerman, A. S., Kirkpatrick, M. P., Stevens, D. E., and Toon, O. B.: The Impact of Humidity above Stratiform Clouds on Indirect Aerosol Climate Forcing, Nature, 432, 1014–1017, https://doi.org/10.1038/nature03174, 2004.

Ackerman, A. S., vanZanten, M. C., Stevens, B., Savic-Jovcic, V., Bretherton, C. S., Chlond, A., Golaz, J.-C., Jiang, H., Khairoutdinov, M., Krueger, S. K., Lewellen, D. C., Lock, A., Moeng, C.-H., Nakamura, K., Petters, M. D., Snider, J. R., Weinbrecht, S., and Zulauf, M.: Large-Eddy Simulations of a Drizzling, Stratocumulus-Topped Marine Boundary Layer, Monthly Weather Review, 137, 1083–1110, https://doi.org/10.1175/2008MWR2582.1, 2009.

Albrecht, B. A.: Aerosols, Cloud Microphysics, and Fractional Cloudiness, Science, 245, 1227–1230, https://doi.org/10.1126/science.245.4923.1227, 1989.

Bašták Ďurán, I., Sakradzija, M., and Schmidli, J.: The Two-Energies Turbulence Scheme Coupled to the Assumed PDF Method, Journal of Advances in Modeling Earth Systems, 14, e2021MS002 922, https://doi.org/10.1029/2021MS002922, 2022.

Bašták Ďurán, I., Köhler, M., Eichhorn-Müller, A., Maurer, V., Schmidli, J., Schomburg, A., Klocke, D., Göcke, T., Schäfer, S., Schlemmer, L., and Dewani, N.: The ICON Single-Column Mode, Atmosphere, 12, https://doi.org/10.3390/atmos12070906, 2021.

Blahak, U.: New implementation of explicit hydrometeor sedimentation in the Seifert-Beheng 2-moment bulk microphysical scheme, https://www.cosmo-model.org/content/model/documentation/core/docu_sedi_twomom.pdf, accessed: 01.09.25, 2020.

Blossey, P. N., Bretherton, C. S., and Wyant, M. C.: Subtropical Low Cloud Response to a Warmer Climate in a Superparameterized Climate Model. Part II: Column Modeling with a Cloud Resolving Model, Journal of Advances in Modeling Earth Systems, 1, JAMES.2009.1.8, https://doi.org/10.3894/JAMES.2009.1.8, 2009.

Blossey, P. N., Bretherton, C. S., and Mohrmann, J.: Simulating Observed Cloud Transitions in the Northeast Pacific during CSET, Monthly Weather Review, https://doi.org/10.1175/MWR-D-20-0328.1, 2021.

Bolt, S. and Omanovic, N.: Evaluation of Semi-Implicit and Explicit Sedimentation Approaches in the Two-Moment Cloud Microphysics Scheme of ICON, Geoscientific Model Development, 19, 595–619, https://doi.org/10.5194/gmd-19-595-2026, 2026.

Brendecke, J., Dong, X., Xi, B., and Zheng, X.: Maritime Aerosol and CCN Profiles Derived From Ship-Based Measurements Over Eastern North Pacific During MAGIC, Earth and Space Science, 9, e2022EA002 319, https://doi.org/10.1029/2022EA002319, 2022.

Bretherton, C. S. and Wyant, M. C.: Moisture Transport, Lower-Tropospheric Stability, and Decoupling of Cloud-Topped Boundary Layers, Journal of the Atmospheric Sciences, 54, 148–167, https://doi.org/10.1175/1520-0469(1997)054<0148:MTLTSA>2.0.CO;2, 1997.

Bretherton, C. S., Blossey, P. N., and Uchida, J.: Cloud Droplet Sedimentation, Entrainment Efficiency, and Subtropical Stratocumulus Albedo, Geophysical Research Letters, 34, 2006GL027 648, https://doi.org/10.1029/2006GL027648, 2007.

Bretherton, C. S., McCoy, I. L., Mohrmann, J., Wood, R., Ghate, V., Gettelman, A., Bardeen, C. G., Albrecht, B. A., and Zuidema, P.: Cloud, Aerosol, and Boundary Layer Structure across the Northeast Pacific Stratocumulus–Cumulus Transition as Observed during CSET, Monthly Weather Review, 147, 2083–2103, https://doi.org/10.1175/MWR-D-18-0281.1, 2019.

Christensen, M. W., Jones, W. K., and Stier, P.: Aerosols Enhance Cloud Lifetime and Brightness along the Stratus-to-Cumulus Transition, Proceedings of the National Academy of Sciences, 117, 17 591–17 598, https://doi.org/10.1073/pnas.1921231117, 2020.

de Lozar, A. and Mellado, J. P.: Reduction of the Entrainment Velocity by Cloud Droplet Sedimentation in Stratocumulus, Journal of the Atmospheric Sciences, 74, 751–765, https://doi.org/10.1175/JAS-D-16-0196.1, 2017.

https://doi.org/10.5194/egusphere-2026-479
Preprint. Discussion started: 29 January 2026

De Roode, S. R., Sandu, I., Van Der Dussen, J. J., Ackerman, A. S., Blossey, P., Jarecka, D., Lock, A., Siebesma, A. P., and Stevens, B.: Large-Eddy Simulations of EUCLIPSE–GASS Lagrangian Stratocumulus-to-Cumulus Transitions: Mean State, Turbulence, and Decoupling, Journal of the Atmospheric Sciences, 73, 2485–2508, https://doi.org/10.1175/JAS-D-15-0215.1, 2016.

Dhandapani, C., Kaul, C. M., Pressel, K. G., Blossey, P. N., Wood, R., and Kulkarni, G.: Sensitivities of Large Eddy Simulations of Aerosol Plume Transport and Cloud Response, Journal of Advances in Modeling Earth Systems, 17, e2024MS004 546, https://doi.org/10.1029/2024MS004546, 2025.

Dipankar, A., Stevens, B., Heinze, R., Moseley, C., Zängl, G., Giorgetta, M., and Brdar, S.: Large eddy simulation using the general circulation model ICON, Journal of Advances in Modeling Earth Systems, 7, 963–986, https://doi.org/https://doi.org/10.1002/2015MS000431, 2015.

Eastman, R. and Wood, R.: Factors Controlling Low-Cloud Evolution over the Eastern Subtropical Oceans: A Lagrangian Perspective Using the A-Train Satellites, Journal of the Atmospheric Sciences, 73, 331–351, https://doi.org/10.1175/JAS-D-15-0193.1, 2016.

Erfani, E., Blossey, P., Wood, R., Mohrmann, J., Doherty, S. J., Wyant, M., and O, K.-T.: Simulating Aerosol Lifecycle Impacts on the Subtropical Stratocumulus-to-Cumulus Transition Using Large-Eddy Simulations, Journal of Geophysical Research: Atmospheres, 127, e2022JD037 258, https://doi.org/10.1029/2022JD037258, 2022.

Feingold, G., Cotton, W. R., Kreidenweis, S. M., and Davis, J. T.: The Impact of Giant Cloud Condensation Nuclei on Drizzle Formation in Stratocumulus: Implications for Cloud Radiative Properties, Journal of the Atmospheric Sciences, 56, 4100–4117, https://doi.org/10.1175/1520-0469(1999)056<4100:TIOGCC>2.0.CO;2, 1999.

Feingold, G., Koren, I., Yamaguchi, T., and Kazil, J.: On the Reversibility of Transitions between Closed and Open Cellular Convection, Atmospheric Chemistry and Physics, 15, 7351–7367, https://doi.org/10.5194/acp-15-7351-2015, 2015.

Hill, A. A., Feingold, G., and Jiang, H.: The Influence of Entrainment and Mixing Assumption on Aerosol–Cloud Interactions in Marine Stratocumulus, Journal of the Atmospheric Sciences, 66, 1450–1464, https://doi.org/10.1175/2008JAS2909.1, 2009.

Hogan, R. and Bozzo, A.: A flexible and efficient radiation scheme for the ECMWF model: A flexible radiation scheme for the ECMWF model, Journal of Advances in Modeling Earth Systems, 10, https://doi.org/10.1029/2018MS001364, 2018.

Igel, A. L.: Processes Controlling the Entrainment and Liquid Water Response to Aerosol Perturbations in Nonprecipitating Stratocumulus Clouds, https://doi.org/10.1175/JAS-D-23-0238.1, 2024.

Keeler, E., Burk, K., and Kyrouac, J.: Balloon-Borne Sounding System (SONDEWNPN), 2012-10-01 to 2013-10-03, ARM Mobile Facility (MAG), Los Angeles, CA to Honolulu, HI - container ship Horizon Spirit; AMF2 (M1), https://doi.org/10.5439/1595321.

Klein, S. A. and Hartmann, D. L.: The Seasonal Cycle of Low Stratiform Clouds, https://journals.ametsoc.org/view/journals/clim/6/8/1520-0442_1993_006_1587_tscols_2_0_co_2.xml, 1993.

Krueger, S. K., McLean, G. T., and Fu, Q.: Numerical Simulation of the Stratus-to-Cumulus Transition in the Subtropical Marine Boundary Layer. Part II: Boundary-Layer Circulation, https://journals.ametsoc.org/view/journals/atsc/52/16/1520-0469_1995_052_2851_nsotst_2_0_co_2.xml, 1995.

Lilly, D. K.: On the numerical simulation of buoyant convection, Tellus, 14, 148–172, https://doi.org/10.3402/tellusa.v14i2.9537, 1962.

Lilly, D. K.: Models of cloud-topped mixed layers under a strong inversion, Quarterly Journal of the Royal Meteorological Society, 94, 292–309, https://doi.org/https://doi.org/10.1002/qj.49709440106, 1968.

Louis, J.-F.: A parametric model of vertical eddy fluxes in the atmosphere, Boundary-Layer Meteorology, 17, 187–202, 1979.

https://doi.org/10.5194/egusphere-2026-479
Preprint. Discussion started: 29 January 2026

McGibbon, J. and Bretherton, C. S.: Skill of ship-following large-eddy simulations in reproducing MAGIC observations across the northeast Pacific stratocumulus to cumulus transition region, Journal of Advances in Modeling Earth Systems, 9, 810–831, https://doi.org/https://doi.org/10.1002/2017MS000924, 2017.

Minnis, P., Nguyen, L., Doelling, D. R., Young, D. F., Miller, W. F., and Kratz, D. P.: Rapid Calibration of Operational and Research Meteorological Satellite Imagers. Part I: Evaluation of Research Satellite Visible Channels as References, Journal of Atmospheric and Oceanic Technology, 19, 1233–1249, https://doi.org/10.1175/1520-0426(2002)019<1233:RCOOAR>2.0.CO;2, 2002.

Minnis, P., Nguyen, L., Palikonda, R., Heck, P. W., Spangenberg, D. A., Doelling, D. R., Ayers, J. K., Jr., W. L. S., Khaiyer, M. M., Trepte, Q. Z., Avey, L. A., Chang, F.-L., Yost, C. R., Chee, T. L., and Szedung, S.-M.: Near-real time cloud retrievals from operational and research meteorological satellites, in: Remote Sensing of Clouds and the Atmosphere XIII, edited by Picard, R. H., Comeron, A., Schäfer, K., Amodeo, A., and van Weele, M., vol. 7107, p. 710703, International Society for Optics and Photonics, SPIE, https://doi.org/10.1117/12.800344, 2008.

Minnis, P., Sun-Mack, S., Young, D. F., Heck, P. W., Garber, D. P., Chen, Y., Spangenberg, D. A., Arduini, R. F., Trepte, Q. Z., Smith, W. L., Ayers, J. K., Gibson, S. C., Miller, W. F., Hong, G., Chakrapani, V., Takano, Y., Liou, K.-N., Xie, Y., and Yang, P.: CERES Edition-2 Cloud Property Retrievals Using TRMM VIRS and Terra and Aqua MODIS Data—Part I: Algorithms, IEEE Transactions on Geoscience and Remote Sensing, 49, 4374–4400, https://doi.org/10.1109/TGRS.2011.2144601, 2011.

Mohrmann, J., Bretherton, C. S., McCoy, I. L., McGibbon, J., Wood, R., Ghate, V., Albrecht, B., Sarkar, M., Zuidema, P., and Palikonda, R.: Lagrangian Evolution of the Northeast Pacific Marine Boundary Layer Structure and Cloud during CSET, Monthly Weather Review, 147, 4681–4700, https://doi.org/10.1175/MWR-D-19-0053.1, 2019.

Murakami, Y., Kummerow, C. D., and Van Den Heever, S. C.: On the Relation among Satellite Observed Liquid Water Path, Cloud Droplet Number Concentration and Cloud Base Rain Rate and Its Implication to the Auto-Conversion Parameterization in Stratocumulus Clouds, Journal of Climate, p. 1, https://doi.org/10.1175/JCLI-D-20-0473.1, 2021.

Painemal, D., Minnis, P., and Nordeen, M.: Aerosol Variability, Synoptic-Scale Processes, and Their Link to the Cloud Microphysics over the Northeast Pacific during MAGIC, Journal of Geophysical Research: Atmospheres, 120, 5122–5139, https://doi.org/10.1002/2015JD023175, 2015.

Pistor, R. and Mellado, J. P.: Resolving Droplet Sedimentation Effects in Stratocumulus Clouds, Journal of Advances in Modeling Earth Systems, 17, e2025MS004 966, https://doi.org/10.1029/2025MS004966, 2025.

Pruppacher, H. R. and Klett, J. D.: Microphysics of Clouds and Precipitation, Springer Dordrecht, 1997.

Rossow, W. B. and Schiffer, R. A.: Advances in Understanding Clouds from ISCCP, Bulletin of the American Meteorological Society, 80, 2261–2288, https://doi.org/10.1175/1520-0477(1999)080<2261:AIUCFI>2.0.CO;2, 1999.

Sandu, I. and Stevens, B.: On the Factors Modulating the Stratocumulus to Cumulus Transitions, Journal of the Atmospheric Sciences, 68, 1865–1881, https://doi.org/10.1175/2011JAS3614.1, 2011.

Sandu, I., Stevens, B., and Pincus, R.: On the Transitions in Marine Boundary Layer Cloudiness, Atmos. Chem. Phys., 2010.

Sarkar, M., Zuidema, P., Albrecht, B., Ghate, V., Jensen, J., Mohrmann, J., and Wood, R.: Observations Pertaining to Precipitation within the Northeast Pacific Stratocumulus-to-Cumulus Transition, Monthly Weather Review, 148, 1251–1273, https://doi.org/10.1175/MWR-D-19-0235.1, 2019.

Savic-Jovcic, V. and Stevens, B.: The Structure and Mesoscale Organization of Precipitating Stratocumulus, Journal of the Atmospheric Sciences, 65, 1587–1605, https://doi.org/10.1175/2007JAS2456.1, 2008.

https://doi.org/10.5194/egusphere-2026-479
Preprint. Discussion started: 29 January 2026

Schulz, B. and Mellado, J. P.: Competing Effects of Droplet Sedimentation and Wind Shear on Entrainment in Stratocumulus, Journal of Advances in Modeling Earth Systems, 11, 1830–1846, https://doi.org/10.1029/2019MS001617, 2019.

Seifert, A. and Beheng, K. D.: A two-moment cloud microphysics parameterization for mixed-phase clouds. Part 1: Model description, Meteorology and Atmospheric Physics, 92, 45–66, https://doi.org/10.1007/s00703-005-0112-4, 2006.

Smagorinsky, J.: General Circulation Experiments with the Primitive Equations, Monthly Weather Review, 91, 99 – 164, https://doi.org/10.1175/1520-0493(1963)091<0099:GCEWTP>2.3.CO;2, 1963.

Stephens, G. L.: Radiation Profiles in Extended Water Clouds. II: Parameterization Schemes, 1978.

Stevens, B., Cotton, W. R., Feingold, G., and Moeng, C.-H.: Large-Eddy Simulations of Strongly Precipitating, Shallow, Stratocumulus-Topped Boundary Layers, Journal of the Atmospheric Sciences, 55, 3616–3638, https://doi.org/10.1175/1520-0469(1998)055<3616:LESOSP>2.0.CO;2, 1998.

Stevens, B., Moeng, C.-H., Ackerman, A. S., Bretherton, C. S., Chlond, A., de Roode, S., Edwards, J., Golaz, J.-C., Jiang, H., Khairoutdinov, M., Kirkpatrick, M. P., Lewellen, D. C., Lock, A., Müller, F., Stevens, D. E., Whelan, E., and Zhu, P.: Evaluation of Large-Eddy Simulations via Observations of Nocturnal Marine Stratocumulus, Monthly Weather Review, 133, 1443–1462, https://doi.org/10.1175/MWR2930.1, 2005.

Szczap, F., Gour, Y., Fauchez, T., Cornet, C., Faure, T., Jourdan, O., Penide, G., and Dubuisson, P.: A Flexible Three-Dimensional Stratocumulus, Cumulus and Cirrus Cloud Generator (3DCLOUD) Based on Drastically Simplified Atmospheric Equations and the Fourier Transform Framework, Geoscientific Model Development, 7, 1779–1801, https://doi.org/10.5194/gmd-7-1779-2014, 2014.

Turner, D. D., Vogelmann, A. M., Austin, R. T., Barnard, J. C., Cady-Pereira, K., Chiu, J. C., Clough, S. A., Flynn, C., Khaiyer, M. M., Liljegren, J., Johnson, K., Lin, B., Long, C., Marshak, A., Matrosov, S. Y., McFarlane, S. A., Miller, M., Min, Q., Minimis, P., O'Hirok, W., Wang, Z., and Wiscombe, W.: Thin Liquid Water Clouds: Their Importance and Our Challenge, Bulletin of the American Meteorological Society, 88, 177–190, https://doi.org/10.1175/BAMS-88-2-177, 2007.

Twomey, S.: The Influence of Pollution on the Shortwave Albedo of Clouds, 1977.

Twomey, S. A., Piepgrass, M., and Wolfe, T. L.: An assessment of the impact of pollution on global cloud albedo, Tellus B, 36B, 356–366, https://doi.org/https://doi.org/10.1111/j.1600-0889.1984.tb00254.x, 1984.

Williams, A. S. and Igel, A. L.: Cloud Top Radiative Cooling Rate Drives Non-Precipitating Stratiform Cloud Responses to Aerosol Concentration, Geophysical Research Letters, 48, e2021GL094 740, https://doi.org/10.1029/2021GL094740, 2021.

Wood, R.: Stratocumulus Clouds, Monthly Weather Review, 140, 2373–2423, https://doi.org/10.1175/MWR-D-11-00121.1, 2012.

Wood, R., O, K.-T., Bretherton, C. S., Mohrmann, J., Albrecht, Bruce. A., Zuidema, P., Ghate, V., Schwartz, C., Eloranta, E., Glienke, S., Shaw, R. A., Fugal, J., and Minnis, P.: Ultraclean Layers and Optically Thin Clouds in the Stratocumulus-to-Cumulus Transition. Part I: Observations, Journal of the Atmospheric Sciences, 75, 1631–1652, https://doi.org/10.1175/JAS-D-17-0213.1, 2018.

Wyant, M. C., Bretherton, C. S., Rand, H. A., and Stevens, D. E.: Numerical Simulations and a Conceptual Model of the Stratocumulus to Trade Cumulus Transition, Journal of the Atmospheric Sciences, 54, 168–192, https://doi.org/10.1175/1520-0469(1997)054<0168:NSAACM>2.0.CO;2, 1997.

Wyant, M. C., Bretherton, C. S., Chlond, A., Griffin, B. M., Kitagawa, H., Lappen, C.-L., Larson, V. E., Lock, A., Park, S., de Roode, S. R., Uchida, J., Zhao, M., and Ackerman, A. S.: A Single-Column Model Intercomparison of a Heavily Drizzling Stratocumulus-Topped Boundary Layer, Journal of Geophysical Research: Atmospheres, 112, https://doi.org/10.1029/2007JD008536, 2007.

Yamaguchi, T., Feingold, G., and Kazil, J.: Stratocumulus to Cumulus Transition by Drizzle, Journal of Advances in Modeling Earth Systems, 9, 2333–2349, https://doi.org/10.1002/2017MS001104, 2017.

https://doi.org/10.5194/egusphere-2026-479
Preprint. Discussion started: 29 January 2026

Zhang, D., Ermold, B., and Morris, V.: Ceilometer (CEIL), 2012-10-01 to 2013-09-26, ARM Mobile Facility (MAG), Los Angeles, CA to Honolulu, HI - container ship Horizon Spirit; AMF2 (M1), https://doi.org/10.5439/1181954.

Zheng, X., Klein, S. A., Ghate, V. P., Santos, S., McGibbon, J., Caldwell, P., Bogenschutz, P., Lin, W., and Cadeddu, M. P.: Assessment of Precipitating Marine Stratocumulus Clouds in the E3SMv1 Atmosphere Model: A Case Study from the ARM MAGIC Field Campaign, Monthly Weather Review, 148, 3341–3359, https://doi.org/10.1175/MWR-D-19-0349.1, 2020.

Zhou, X., Kollias, P., and Lewis, E. R.: Clouds, Precipitation, and Marine Boundary Layer Structure during the MAGIC Field Campaign, Journal of Climate, 28, 2420–2442, https://doi.org/10.1175/JCLI-D-14-00320.1, 2015.

Zängl, G., Reinert, D., Rípodas, P., and Baldauf, M.: The ICON (ICOsahedral Non-hydrostatic) modelling framework of DWD and MPI-M: Description of the non-hydrostatic dynamical core, Quarterly Journal of the Royal Meteorological Society, 141, 563–579, https://doi.org/https://doi.org/10.1002/qj.2378, 2015.